PAPER • OPEN ACCESS

Exploring extreme magnetization phenomena in directly driven imploding cylindrical targets

To cite this article: C A Walsh *et al* 2022 *Plasma Phys. Control. Fusion* **64** 025007

View the article online for updates and enhancements.

Exploring extreme magnetization phenomena in directly driven imploding cylindrical targets

C A Walsh[1],*(iD), R Florido[2](iD), M Bailly-Grandvaux[3](iD), F Suzuki-Vidal[4], J P Chittenden[4], A J Crilly[4], M A Gigosos[5], R C Mancini[6], G Pérez-Callejo[7](iD), C Vlachos[7](iD), C McGuffey[8], F N Beg[8](iD) and J J Santos[7](iD)

[1] Lawrence Livermore National Laboratory, Livermore, CA, United States of America
[2] iUNAT—Departamento de Física, Universidad de Las Palmas de Gran Canaria, 35017 Las Palmas de Gran Canaria, Spain
[3] Center for Energy Research, University of California, San Diego La Jolla, CA, United States of America
[4] Blackett Laboratory, Imperial College London, London SW7 2AZ, United Kingdom
[5] Departamento de Física Teórica, Atómica y Óptica, Universidad de Valladolid, 47071 Valladolid, Spain
[6] Department of Physics, University of Nevada, Reno, NV 89557, United States of America
[7] Université de Bordeaux-CNRS-CEA, Centre Lasers Intenses et Applications (CELIA), UMR 5107, F-33405 Talence, France
[8] General Atomics, San Diego, CA, United States of America

E-mail: walsh34@llnl.gov

CrossMark

Abstract

This paper uses extended-magnetohydrodynamics (MHD) simulations to explore an extreme magnetized plasma regime realizable by cylindrical implosions on the OMEGA laser facility. This regime is characterized by highly compressed magnetic fields (greater than 10 kT across the fuel), which contain a significant proportion of the implosion energy and induce large electrical currents in the plasma. Parameters governing the different magnetization processes such as Ohmic dissipation and suppression of instabilities by magnetic tension are presented, allowing for optimization of experiments to study specific phenomena. For instance, a dopant added to the target gas-fill can enhance magnetic flux compression while enabling spectroscopic diagnosis of the imploding core. In particular, the use of Ar K-shell spectroscopy is investigated by performing detailed non-LTE atomic kinetics and radiative transfer calculations on the MHD data. Direct measurement of the core electron density and temperature would be possible, allowing for both the impact of magnetization on the final temperature and thermal pressure to be obtained. By assuming the magnetic field is frozen into the plasma motion, which is shown to be a good approximation for highly magnetized implosions, spectroscopic diagnosis could be used to estimate which magnetization processes are ruling the implosion dynamics; for example, a relation is given for inferring whether thermally driven or current-driven transport is dominating.

---

* Author to whom any correspondence should be addressed.

1. Introduction

Magnetic fields are of interest in astrophysics, existing in the universe on all scales: from kilometers or less for compact neutron stars up to millions of light years for clusters of galaxies. Natural magnetic fields can exceed the laboratory magnetic fields achieved by many orders of magnitude, with white dwarfs sustaining magnetic fields of up to 10^5 T and the most extreme neutron stars up to 10^9 T [1]. In such compact stars the magnetic fields are strong enough to modify the structure and composition of the star, as well as its radiation properties [2, 3].

In the laboratory, laser-driven plasma compression has been used to amplify initial (seed) magnetic fields [4]; to first order the magnetic field is frozen into the plasma as it compresses. Proton deflectometry has provided a direct measurement of these compressed magnetic fields up to 4 kT in dedicated cylindrical experiments [5, 6]. Novel techniques to generate strong magnetostatic fields $\sim$1–10 s T by either capacitor-bank pulsed discharges [5, 7–9] or intense laser-driven discharges [10–15] have stimulated a growing interest in laser-driven, high-energy-density (HED) systems with embedded magnetic fields.

In inertial confinement fusion (ICF), highly compressed magnetic fields have been demonstrated to contribute to increase implosion performance [16]. The compressed B-field strengths can be enough to magnetize the electron thermal conduction, reducing the energy losses from the hot-spot and resulting in hotter fuel [17, 18]. The B-fields can also effectively confine D-T ions and thermonuclear α-particles [19], enhancing collisionality and fusion yield. In addition, large magnetic fields can reduce hydrodynamic instabilities through magnetic tension [17, 18, 20–22], although there are also mechanisms that increase perturbation growth with magnetization [18, 23].

Cylindrical geometry provides a simple test bed for exploring magnetized phenomena in HED plasmas, as magnetic fields can increase asymmetry in spherical implosions [18, 23]. In this scheme, the cylinder axis is parallel to the applied B-field direction. Using this geometry, the MagLIF concept was first proposed at Sandia National Laboratories (SNL) in 2010 [24]. It consists of laser pre-heat of cold fuel inside a Z-pinch cylindrical liner (initially with an axial B-field) which is magnetically compressed by a $\sim$20 MA, 150 ns electrical current. Due to fuel magnetization and pre-heating, MagLIF aims at near-adiabatic stable cylindrical compression with lower implosion velocity ($\sim$100 km s^{-1}, instead of >300 km s^{-1}) and lower convergence ratios than conventional ICF. MagLIF has shown promising results through different experimental campaigns by demonstrating thermonuclear neutron generation at fusion-relevant conditions, a high enough fuel magnetization for α-particles trapping [25–27] and reporting first performance scaling studies [28].

A laser-driven approach to MagLIF is being explored at the OMEGA Laser facility [29–33] to provide a test for MagLIF scaling. The driving laser energy is $1000\times$ less than that delivered on the Z-pinch facility at SNL and therefore the laser targets are $10\times$ smaller than on Z. Yet, OMEGA provides a significantly higher repetition rate and better diagnostic access, facilitating the parametric study of the underlying basic physics. Cylindrical implosions are easier to perform and offer a clear axis for diagnostics, as well as for a laser preheat [30] or a fast ignition beam. A recent series of laser-driven experiments [33] used the improved MIFEDS [5, 9] to deliver a seed B-field of nearly 30 T, which was high enough to demonstrate the effects of magnetic pressure decreasing plasma compression. There are prospects to deliver even higher B-field values ($\sim$50 T) within the next few years.

The design and interpretation of all above experiments and applications strongly rely on magnetohydrodynamic (MHD) codes. Simulations must include extended-MHD effects, which represent the transport of energy and magnetic flux in a plasma [34]. Magnetized plasmas are thought to exhibit complex behaviour in the electron population and, above resistive-MHD, extended-MHD additionally accounts for temperature-gradient-driven transport—such as the Nernst term moving magnetic fields down electron temperature gradients—and electric-current-driven transport—such as the Hall term moving magnetic fields with the flow of charge. The Nernst term, in particular, is of great interest to the scientific community, with importance in a broad range of experiments [16, 28, 35–37] with expectations of plasma demagnetization [23, 38–41]. Even with its wide applicability, Nernst advection of magnetic field is yet to be directly measured.

This paper explores the development of extreme magnetization phenomena in directly-driven imploding cylindrical targets using extended-MHD simulations. The starting point for the design is a previous laser-driven implosion on OMEGA (without any fuel pre-heat), which found evidence of significant magnetic pressure during target stagnation [33]. Distinct magnetization phenomena are outlined for this high B-field regime, which can be categorized as related to magnetic field amplification, electron magnetization or induced electrical currents; metrics governing which phenomena are significant are summarized in table 1. Initial target conditions are varied to transition between different regimes; for example, the concentration of a dopant added to the imploding fuel can be increased to amplify magnetic field compression at the expense of electron magnetization, while enabling a spectroscopic characterization of plasma conditions. In particular, the feasibility of Ar K-shell spectroscopy [42–48] for diagnosing the core conditions in magnetized cylindrical implosions is demonstrated by post-processing the extended-MHD simulations and performing non-LTE atomic kinetics and radiative transfer calculations. By using the frozen-in-flow

approximation, a spectroscopic diagnosis of core conditions would allow for estimates of the magnetization metrics.

This paper is organized as follows. Section 2 briefly summarizes the main features of the Gorgon code used to perform the extended-MHD simulations. Section 3 discusses the platform for magnetized direct-drive cylindrical implosions and the corresponding nominal target design. Section 4 discusses key magnetization phenomena that may occur in a magnetized compressed hot-spot. Non-dimensional parameters to quantify the relative importance of different physical processes for any given implosion are introduced. Section 5 uses the metrics defined in section 4 to modify the point-of-design to explore specific physics regimes and scenarios; e.g. maximizing the magnetic field strength requires a different design to maximizing the electron magnetization. Synthetic images of time-resolved Ar K-shell spectra are presented in section 6 in an effort to mimic potential measurements recorded by a streaked spectrometer. Lastly, the appendix compares synthetic proton radiographs produced with Gorgon to experimental data recorded in the cylindrical implosions described in [5, 6], thus validating the basic magnetic transport processes in the code. Sensitivity of the radiographs to magnetic transport by bulk plasma motion and Nernst demagnetization is observed.

2. Gorgon extended-MHD code

The simulations presented in this paper utilize the Gorgon extended-MHD code [41, 49, 50]. The magnetic transport in Gorgon is governed by [34, 51, 67]:

$$\frac{\partial \underline{B}}{\partial t} = -\nabla \times \frac{\eta}{\mu_0} \nabla \times \underline{B} + \nabla \times (\underline{v}_B \times \underline{B}) \\ + \nabla \times \left(\frac{\nabla P_e}{e n_e} - \frac{\beta_\parallel \nabla T_e}{e} \right).$$

(1)

The first term on the right is resistive diffusion with diffusivity η. The second term represents advection of magnetic flux at a velocity $\underline{v}_B$. The final term is the production of magnetic fields due to the Biermann Battery effect and ionization gradients [36, 41, 52–54]. The advection velocity v_B incorporates magnetic fields moving with the plasma bulk motion, the electron heat-flow (the so-called Nernst effect) and with the electrical currents:

$$\underline{v}_B = \underline{v} - \gamma_\perp \nabla T_e - \gamma_\wedge (\hat{\underline{b}} \times \nabla T_e) - \frac{\underline{j}}{e n_e}(1 + \delta_\perp^c) + \frac{\delta_\wedge^c}{e n_e}(\underline{j} \times \hat{\underline{b}}),$$

(2)

where η, β, γ and δ are transport coefficients given by [51]. The coefficients preserve physical behaviour at low magnetization, which can give significant differences [55] to the coefficients calculated by Epperlein and Haines [56]. The processes in equation (2) will be discussed in more detail in section 4. The thermal conduction algorithm is specifically designed for anisotropic heat-flow [57, 58]. Importantly for this work, the plasma dynamics include the Lorentz force and Ohmic dissipation.

Gorgon results have been compared with magnetized cylindrical implosion experiments on OMEGA [5, 6] using synthetic proton radiography, matching the peak proton deflection (and therefore the compressed magnetic field)—details are shown in the appendix. This provides a crucial benchmark for the code and lends additional confidence in using the Gorgon code for the experimental design addressed here, where the main differences are in the increased applied magnetic field and more sophisticated diagnostics (presence of a dopant for spectroscopic purposes). Gorgon simulations of pre-magnetized capsules with 3D perturbations have also been used to study how differing magnetization effects impact on short and long wavelength perturbations, as well as the impact of magnetization on stagnation temperatures and yields [18, 23].

The laser drive is modelled using a ray-trace package and inverse Bremsstrahlung absorption. The simulations in this paper are predominantly 2D, with two demonstrative 3D simulations in section 4. The 2D simulations are in cylindrical geometry $r - z$, such that the axial plasma end losses are captured.

Gorgon uses a $P\frac{1}{3}$ automatic flux-limiting scheme for the radiation transport [59], which captures both the free-streaming and diffusive limits. As Ar-doped D_2 is used to fill the targets, 100 energy groups are considered in order to capture the complex dependence of argon opacity and emissivity on radiation energy, for different concentrations of dopant. It is assumed that the dopant only affects the radiative properties of the fuel, with any changes to the equation of state or electron transport coefficients not incorporated. Going from 0% to 0.65% argon should result in the maximum ionization increasing from 1.00 to 1.11, which can increase (for example) the thermal conductivity by 5%. These changes were assessed using a small number of 1D simulations and were found to have no significant impact on the results.

Thermal and Nernst flux limiters of 0.1 are used throughout this paper. The simulations are run with a radial resolution of $\frac{1}{2}$ μm, which is required in order to resolve the small converged hot-spot size, with final hot-spot diameters on the order of 10–20 μm [33]. Gradients in the axial direction are much shallower, allowing for a converged resolution of 2 μm.

The Gorgon simulations assume that the plasma transport is localized. This is not the case in the laser absorption region [39], although this is not of great importance to this paper. The conditions in the cylindrical hot-spot have been assessed, with electron mean free paths of less than 0.2 μm in the unmagnetized 0.175% Ar dopant concentration case; this indicates that an electron will undergo a number of collisions before transporting its energy out of the >7 μm radius hot-spot. The electron-ion collision time is calculated to be less than 0.01 ps, which is much smaller than the ≈100 ps stagnation time-scale. An applied magnetic field localizes the electrons, with the Larmor radius replacing the mean-free path as the appropriate metric. For compressed fields of 1000 T (a factor of 100 below the peak compression simulated), the electrons are confined to a radius between 0.18 and 0.32 μm for the temperature range 2–6 keV.
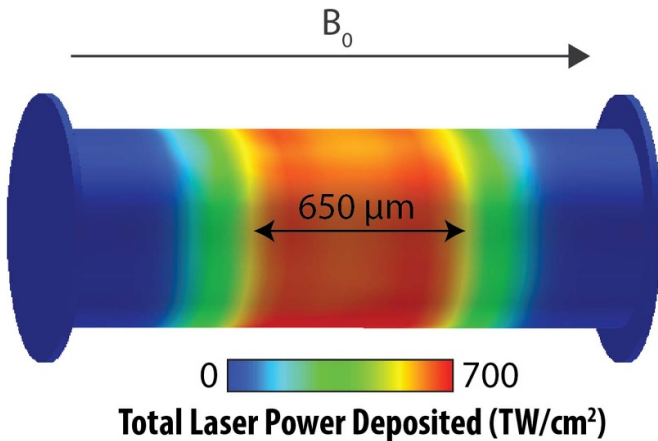
Figure 1. VISRAD image showing the intensity radiation pattern delivered by 40 OMEGA beams on a cylindrical target with an outer radius of 290 μm (see text for details). A nearly uniform irradiation close to 700 TW cm^{-2} is expected on the central $\sim$650 μm-length portion along the cylinder axis.

3. Magnetized cylindrical implosions on OMEGA

While spherical laser-driven implosions are used to obtain high yields, the application of a magnetic field results in anisotropic implosions [18, 23], with the magnetic field normal to the ablator at the pole and in the plane of the ablator at the waist; i.e. a magnetized spherical implosion is intrinsically two-dimensional in its evolution. It was also found that a magnetic field normal to the ablator surface can increase perturbation growth from laser non-uniformities [23]. Therefore, by using a cylindrical target with applied field along the axis, these complications are avoided; the magnetic field is allowed to be everywhere in the plane of the ablator, resulting in a one-dimensional implosion geometry before realistic asymmetries are taken into account. Also, while there is more mass compression in a spherical implosion, the magnetic field is not compressed at the poles, so that effective magnetic field compression is similar between the two geometries.

The nominal target design from recent laser-driven MagLIF implosions (mini-MagLIF campaign) performed at OMEGA is chosen [33], i.e. targets are cylindrical shells made of parylene-N with a density of 1.11 g cm^{-3}, with an outer radius of 290 μm and a wall-thickness of 17 μm. The targets are filled with deuterium at a pressure of 11 atm, i.e. a mass density of 1.81 kg m^{-3}. Targets are imploded by 40 OMEGA beams, delivering a total of 14.5 kJ over 1.5 ns square-shaped pulses. The laser pointing has been empirically optimized to achieve a uniform implosion velocity over an axial extent greater than 600 μm [31, 60]. Figure 1 shows a VISRAD [61] image with the expected laser power irradiation pattern on target; this illumination is used as an input to the Gorgon simulations.

While the present simulation study originates from the mini-MagLIF platform it is worth noting that, in contrast, the goal here is not to find the regime of maximum fusion performance. The approach is to demonstrate that a regime of extreme magnetization is attainable and investigate how the variation of different target parameters can be used to test complex MHD phenomena. For instance, in this work fuel pre-heating is intentionally not considered as it increases the thermal pressure of the hot-spot at the cost of reducing B-field compressibility. Pre-heating is otherwise essential in the MagLIF design to enhance the neutron yield [28]. Therefore, the proposed research is distinct—albeit complementary—to the current mini-MagLIF studies.

As illustration, figure 2 shows simulation results for this setup using a 0.325% argon dopant by deuterium atom. On the left is the density and electron temperature without an applied magnetic field, while the right shows the same properties when a 50 T seed B-field is applied. The snapshot is at 1.45 ns, which is 50 ps before the time of peak neutron production. The hot-spot temperature is greatly enhanced by magnetization, as the electron thermal losses are suppressed perpendicular to the applied field. The core hot-spot density is also greatly decreased by magnetization; this is due to two factors. Firstly, changes in thermal conduction do not change the overall hot-spot thermal pressure [62]. Therefore, an increased temperature by electron magnetization results in a lower density. Secondly, the final total pressure is the sum of thermal and magnetic components; as the magnetic pressure increases, the stagnated thermal pressure decreases, reducing hot-spot compression.

Simulations show that the irradiation pattern of figure 1 drives an implosion with a central $\sim$ 400 μm-long portion for which core conditions show very little variations in the axial direction. This can be seen in figure 2 at the corresponding time of 1.45 ns, but the same behaviour is found over the entire implosion evolution.

As the magnetic flux is compressed along with the plasma, the B-field is strongest in the stagnated fuel. The field strength is greater than 10 kT throughout the D$_2$ plasma when an initial 50 T field is applied to the target. While the outer core is denser than its central portion, i.e. the hot-spot, the magnetic field is able to diffuse over the short radial core length-scales, resulting in a relatively uniform magnetic field throughout the fuel.

Figure 3 shows the temporal evolution of the implosions by plotting the instantaneous neutron-averaged ion temperature and mass density, e.g. the burn-averaged ion temperature is the ion temperature that a fusing D-D reaction sees (a spatial and temporal average). The burn-average is chosen as it weights the properties to those occurring in the hot-spot, where the extreme magnetization phenomena typically take place. Cases with and without a 50 T seed applied field are shown, as well as for two argon dopant concentrations. Clearly the compressed magnetic field enhances the temperature but significantly decreases the hot-spot density. The increased dopant also results in more radiated energy, lowering the temperature but enhancing the compression of hot-spot mass. When compared to unmagnetized implosions, the compression of the imposed B-field has a significant impact on the conditions of the imploding core, which leads to different regimes of extreme magnetization. This raises the question about how to measure and characterize the corresponding magnetization scenario in an implosion experiment. A detailed assessment
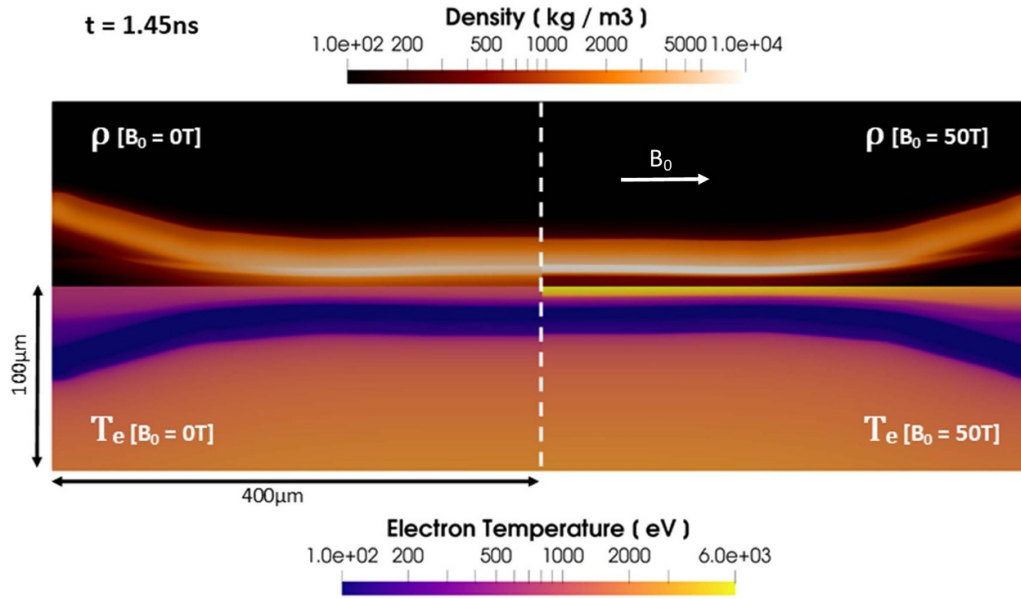
Figure 2. Density (top) and electron temperature (bottom) for 2D MHD Gorgon simulations of deuterium-filled cylindrical implosions with no magnetic field applied (left) and a 50 T seed magnetic field applied (right). The deuterium fuel has an argon dopant with a concentration of 0.325% by atom. The data is shown at 1.45 ns, which is approximately 50 ps before the time of peak neutron production.

about the use of Ar K-shell spectroscopy for this purpose is addressed in section 6.

4. Magnetization phenomena and associated metrics

This section outlines the processes of interest in a magnetized implosion. These phenomena can be split into three categories: the effectiveness of magnetic flux compression, magnetization of the electron population, and induced electrical currents. Metrics for the relative importance of each phenomenon are presented, with design changes explored in section 5.

Firstly, the process of hot-spot magnetic flux compression is examined. As the work here is primarily interested in the field strength in the compressed hot-spot, discussion of magnetic transport in the laser absorption region is avoided. For an in-depth discussion on this issue, see [23, 63].

In order to reach a large magnetization regime in the hot-spot, efficient magnetic flux compression is required. If the magnetic field is completely frozen into the plasma motion, and the plasma motion is one dimensional, then the magnetic field in the fuel would exactly follow $B_z = B_0 \frac{\rho}{\rho_0}$. Therefore, to quantify how close the magnetic transport is to being frozen into the plasma during the implosion, a *frozen-in-flow factor* is defined:

$$\Gamma = \frac{|\underline{B}|}{B_0} \frac{\rho_0}{\rho}, \tag{3}$$

where a value of $\Gamma < 1$ indicates that some magnetic flux has been lost from the hot-spot. The primary factors that change the magnetic flux compression from frozen-in-flow are resistive diffusion, Nernst advection of magnetic fields down

temperature gradients and axial plasma motion. It will be seen in section 5 that $\Gamma \approx 1$ for highly magnetized implosions. In some cases the magnetic flux compression actually exceeds the frozen-in-flow approximation.

While Γ indicates how much magnetic flux is lost from the hot fuel, maximizing this value does not necessarily help to enhance the magnetic field strength in the hot-spot. For this purpose, the field compression factor is utilized:

$$\Lambda = \frac{|\underline{B}|}{B_0}. \tag{4}$$

For an implosion with effective magnetic flux compression ($\Gamma = 1$) the field compression factor is simply:

$$\Lambda = \frac{\rho}{\rho_0}, \quad \text{if } \Gamma = 1, \tag{5}$$

i.e. the more the plasma is compressed, the more the magnetic field is compressed.

Once the magnetic field is compressed, the electron population can become magnetized, with each electron taking a curved path between collisions. The Hall Parameter $\omega_e \tau_e$ quantifies the number of orbits a typical electron takes between collisions. While linked to the magnetic field strength, the magnetization of electrons is also dependent on the electron temperature and density [64]:

$$\omega_e \tau_e \propto \frac{|\underline{B}| T_e^{3/2}}{n_e}. \tag{6}$$

Again, using the frozen-in-flow assumption, the Hall parameter can be expressed in terms of the initial fill density of the target as well as the applied field strength:
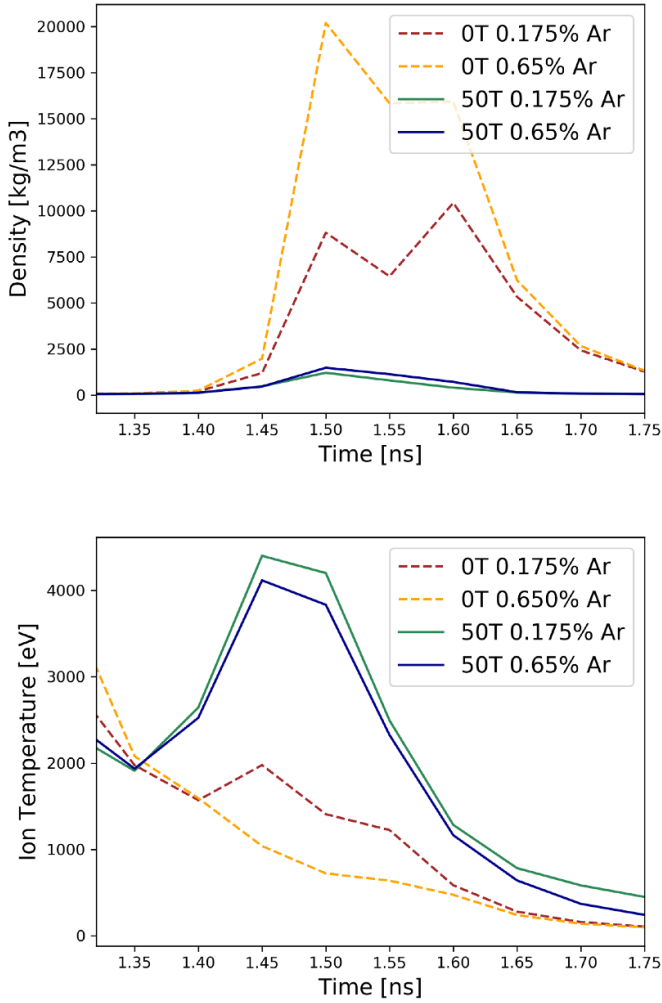
Figure 3. Time history of core conditions from 2D Gorgon simulations of cylindrical implosions as a function of different argon dopant concentrations and applied field strength (see figure 2). Shown values are calculated as instantaneous neutron-averaged quantities, which results in a weighting towards the hot-spot core.

$$\omega_e \tau_e \propto \frac{B_0}{\rho_0} T_e^{3/2}, \quad \text{if } \Gamma = 1. \tag{7}$$

Magnetizing the electron population typically requires much lower magnetic field strengths than magnetic pressure effects [18]. In magnetized fusion experiments, magnetizing the electron population is a primary goal, with thermal conduction suppression resulting in lower energy losses from the fusing plasma [65]. The effect of thermal conduction suppression can be clearly seen in the hot-spot temperature in figure 2 increasing from approximately 1000 to 6000 eV when magnetized (although it will be seen later that a fraction of this increase is due to Ohmic dissipation). In the hot-spot the simulated Hall parameter is in excess of 500, reducing the electron thermal conduction perpendicular to the field lines by a factor of more than 2×10^6.

The Hall parameter also impacts the transport of magnetic fields by the Nernst term. In an extended-MHD plasma, Nernst can be approximated as the advection of magnetic field with the electron heat-flow [34, 55, 66]. Therefore, the extreme

magnetizations simulated in figure 2 result in the suppression of Nernst by a factor greater than 2×10^6, allowing for reduced magnetic flux losses from the hot-spot.

Now the focus turns to induced electrical currents in magnetized implosions. The current takes the form $\underline{j} = \nabla \times \underline{B}/\mu_0$, where the electric field is assumed to vary slowly. Associated with this current is an electron drift velocity $\underline{v}_e = -\underline{j}/en_e$. This drift is expected to result in: the transport of thermal and magnetic energy at velocity $\underline{v}_e$; a dynamically important force; an additional heating term as the finite resistivity of the plasma converts magnetic energy into electron thermal energy. Observing these phenomena experimentally would be an interesting outcome of this platform.

The Lorentz force is recovered by noting that the electron drift is a movement of electrons in a magnetic field $\underline{f} = (\underline{v}_e \times \underline{B})en_e$; a component of this force is the magnetic pressure. In an unmagnetized target the implosion kinetic energy is converted into stagnated thermal energy, with the plasma retaining some residual kinetic energy depending on implosion symmetry. When a large magnetic field is introduced, some of that implosion kinetic energy converts to magnetic energy instead; the imploding shell decelerates on the magnetic pressure rather than the hot-spot pressure. To characterize this, the ratio of the thermal pressure to the magnetic pressure is typically used:

$$\beta = \frac{P_{\text{th}}}{P_{\text{mag}}} = \frac{2(P_e + P_i)\mu_0}{|\underline{B}|^2} \approx \frac{2(n_e T_e + n_i T_i)\mu_0}{|\underline{B}|^2}, \tag{8}$$

where an ideal gas equation of state is assumed for the gas-fill.

For the simulation with a 50 T applied magnetic field in figure 2, the magnetic pressure is approximately equal to the thermal pressure ($\beta \approx 1$). A combination of the substantial magnetic pressure and the heat-flow suppression accounts for the lower hot-spot density in the simulation when a 50 T magnetic field is applied.

Equation (8) can be recast in terms of the initial applied field and gas fill density by assuming $\Gamma = 1$ (i.e frozen-in-flow). Also incorporating the assumption that the ion and electron temperatures are similar gives:

$$\beta = \frac{2(1+Z)\rho_0^2 \, T_e \mu_0}{m_i B_0^2 \, \rho}, \quad \text{if } \Gamma = 1, \tag{9}$$

where Z is the average ionization of the core plasma ($Z = 1$ for deuterium) and m_i is the corresponding ion mass. According to equation (9), a higher temperature hot-spot enhances the thermal pressure, but more compression of the plasma (and therefore magnetic field) enhances the magnetic pressure contribution.

Implosions dominated by magnetic pressure have previously been indirectly inferred in an experiment similar to the configuration discussed here [33]. The neutron yield was seen to increase by approximately 50% going from 0 to 10 T, primarily due to hot-spot thermal losses being reduced. However, going from 10 to 27 T decreased the yield by around 50%. Simulations attributed the decrease to the magnetic pressure

increasing in the hot-spot at the expense of the thermal pressure [33]. While the decrease in thermal pressure is undesirable for reaching high neutron yields, the large magnetic pressure also results in a highly magnetized regime with large induced electrical currents; these currents are of interest to the research proposed here.

Simulations anticipate that an initial 50 T field is amplified to greater than 2×10^4 T. Compressing a magnetic field in excess of 10^4 T in a hot-spot of around $10 \, \mu m$ radius results in a large electric current. For a cylindrical implosion the magnetic field remains predominantly axial, giving a purely azimuthal current that can be approximated as:

$$j_\theta \approx -\frac{B_z}{R_{hs}\mu_0},$$
(10)

where R_{hs} is the hot-spot radius. The final hot-spot radius can also be related to the compressed density with the convergence relation $R_{hs}/R_0 = \sqrt{\rho_0/\rho}$, i.e. mass conservation assumption. Combining this with the frozen-in-flow assumption:

$$j_\theta \approx -\frac{B_0}{\mu_0 \, R_0}\left(\frac{\rho}{\rho_0}\right)^{3/2}, \quad \text{if } \Gamma = 1.$$
(11)

Clearly, a larger initial applied magnetic field and greater plasma compression result in a larger magnitude induced current.

The electrical resistance of the plasma leads to diffusion of the magnetic field. The associated drop in magnetic energy results in additional energy into the electron population (through Ohmic dissipation). For the magnetized simulation in figure 2 this contributes to an enhanced electron temperature that exceeds the ion temperature. When Ohmic dissipation is switched off in the code, the peak electron temperature at bang time drops from 6.0 to 4.2 keV.

The resistive diffusion timescale is:

$$t_{\mathrm{diff}} = \frac{R^2 \, \mu_0}{\eta},$$
(12)

where $\eta = \alpha_\perp^c m_e/(\tau_{ei} e^2 n_e)$ is the magnetic diffusivity and $\alpha_\perp^c$ is the dimensionless resistivity that only depends on plasma magnetization and ionization [51]. The timescale t_{diff} defines both the rate of magnetic field diffusion as well as the Ohmic heating. For plasmas with $\beta \approx 1$ and resistive diffusion timescales on the order of the hot-spot stagnation time ($t_{\mathrm{diff}} \approx t_{\mathrm{stag}}$), the energy exchange from magnetic to electron thermal energy will be significant. Therefore, an Ohmic heating factor Π is defined:

$$\Pi = \frac{t_{\mathrm{stag}}}{t_{\mathrm{diff}}}\frac{1}{\beta}.$$
(13)

Using the convergence relation $R/R_0 = \sqrt{\rho_0/\rho}$ and equations (9), (12) and (13), the Ohmic heating factor can be re-written:

$$\Pi = \frac{B_0}{\rho_0^3}\frac{t_{\mathrm{stag}}\rho}{\tau_{ei}T_e}\alpha_\perp^c\frac{m_i^2 \, m_e Z}{2(Z+1)e}, \quad \text{if } \Gamma = 1.$$
(14)

Note that the diffusion is greatest at the edge of the core, where the fuel is more dense and lower in temperature.

In addition to the resistive diffusion of the magnetic field, the electrical current drives magnetic field advection [34, 67]. Primarily, this is the transport of the magnetic field at the electron drift velocity $\underline{v}_e = \underline{j}/en_e$, but with collisional corrections. The advection of magnetic field with the electron drift velocity is often called the Hall term. There is a similar transport of the electron energy at the electron drift velocity, which here will be called the thermal Hall term. The similarities in the advection velocities can be made clear by writing [34]:

$$\underline{v}_{jB} = -(1+\delta_\perp^c)\frac{\underline{j}_\perp}{en_e} + \delta_\wedge^c\left(\frac{\underline{j}}{en_e}\times\hat{\underline{b}}\right),$$
(15)

$$\underline{v}_{jU_e} = -(1+\beta_\parallel^c)\frac{\underline{j}_\parallel}{en_e} - (1+\beta_\perp^c)\frac{\underline{j}_\perp}{en_e} + \beta_\wedge^c\left(\frac{\underline{j}}{en_e}\times\hat{\underline{b}}\right),$$
(16)

where $\underline{v}_{jB}$ is the advection of magnetic field due to electrical currents and $\underline{v}_{jU_e}$ is the advection of electron energy due to electrical currents, $\underline{j}_\parallel$ represents the component of the current along the magnetic field, and $\underline{j}_\perp$ is the component perpendicular. $\hat{\underline{b}}$ is the magnetic field unit vector. The $\beta_\wedge^c$ term is known as the Ettingshausen heat-flow. Note that there is no advection of magnetic field parallel to the magnetic field itself, as this has no effect on the magnetic field. The dimensionless transport coefficients δ^c and β^c [34] provide collisional corrections to the collisionless current-driven phenomena. The $\delta_\wedge$ coefficient calculated from Epperlein and Haines [56] gives erroneous behaviour at low magnetization; updated polynomial fits are given in [51]. Transport driven by electrical currents has been discussed theoretically in pulsed power plasma experiments [68, 69] and in low density plasma jets [70] but to the best of the authors' knowledge has not been measured experimentally. Current-driven transport has not been shown to be significant in dense laser-driven implosions such as those discussed here.

The Hall (and thermal Hall) velocities are typically larger than the collisional corrections. An approximate expression for this velocity can be found by using equation (11), which assumed a purely axial magnetic field:

$$v_j \approx \frac{B_0}{\mu_0 \, R_0}\frac{\rho^{1/2}}{\rho_0^{3/2}}\frac{m_i}{Ze}.$$
(17)

The drift velocity is larger for a greater applied magnetic field strength. A lower initial fill density ρ_0 also enhances the velocity, as the magnetic field is more easily compressed. Note that these relations must be adapted if studying spherical implosions, as the magnetic field lines are not everywhere perpendicular to the implosion velocity.

A dimensionless number Ξ was defined in [34] as the ratio of the Nernst velocity to the Hall velocity:

$$\Xi = \frac{\gamma_\perp^c \tau_{ei}T_e en_e\mu_0}{|\underline{B}|m_e}.$$
(18)

This ratio is a metric for whether the transport is dominated by temperature gradients or electrical currents. Using burn-averaged quantities the implosion shown in figure 2 has $\Xi <$ 0.002 for an applied field of 50 T. While this shows the current-driven transport dominating over the thermal transport, this is mainly due to the extreme suppression of Nernst at such high magnetizations.

For 2D $r - z$ simulations, the induced electrical current is purely in the azimuthal direction θ, which means there is no compression of magnetic field by advection with the current and exactly no change in the electron energy profile. The collisional corrections to the Hall and thermal Hall can be in the simulation plane (such as the Ettingshausen $\beta_\wedge^c$ term in equation (16)), but these are smaller than the collisionless component. With variations in the axial direction, the Hall term can induce a twist in the magnetic field profile. This can be seen by decomposing the change in magnetic field due to an advection velocity directed in θ:

$$\left[\frac{\partial B_\theta}{\partial t}\right]_{\text{advection}} = B_r \frac{\partial v_{j\theta}}{\partial r} - B_z \frac{\partial v_{j\theta}}{\partial z}. \tag{19}$$

Noting that the magnetic field is dominated by the axial component, a time-scale for twisting the magnetic field can be obtained:

$$t_{\text{twist}} = \frac{L_{hs}}{2v_j}, \tag{20}$$

where L_{hs} is the axial length over which the hot-spot is uniformly driven. Using equations (10), (20) becomes:

$$t_{\text{twist}} = L_{hs} R_{hs} \frac{1}{2} \frac{\rho_0}{B_0} \frac{\mu_0 e Z}{m_i}, \tag{21}$$

i.e. both a small hot-spot radius R_{hs} and length L_{hs} are required for significant magnetic field twisting to occur.

For 2D simulations such as those shown in figure 2, the Hall term has been included. Due to the large uniformly-driven length ($L_{hs} \approx 600\ \mu$m) only marginal twisting of the magnetic field occurs. Over the uniformly-driven central length the field twisting $|B_\theta|/|\underline{B}| \leq 0.01$. Towards the edges, where 2D effects are most important $|B_\theta|/|\underline{B}| \leq 0.1$.

Once the magnetic field is twisted by the Hall term, a component of the induced current emerges in the 2D $r - z$ simulation plane. The electron energy is then affected by the thermal Hall term. A component of the Lorentz force becomes in the θ direction, which may result in rotation of the plasma. Simulations where the uniform hot-spot length L_{hs} is reduced have been attempted, but once significant B_θ field emerges, the simulations become unstable. This may be related to the natural instability of Braginskii's MHD description [71].

The stabilization of perturbation growth by large induced electrical currents is of great interest to magnetized ICF implosions [17, 18, 22]. The cylindrical implosions discussed in this paper could be used as a platform for investigating this behaviour. To demonstrate this, 3D simulations are initialized from 1D once the first shock converges onto the axis of the implosion. At the time of initialization the implosion velocity
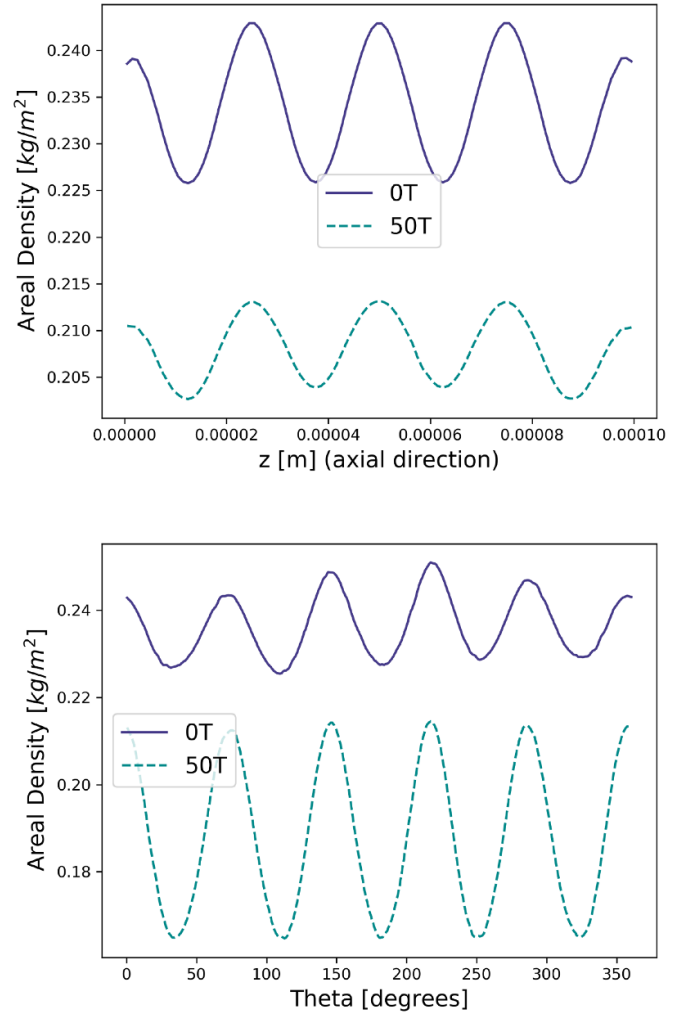

Figure 4. Areal density at time of peak neutron production for 3D Gorgon simulations of cylindrical implosions with an without a 50 T seed magnetic field with artificial velocity perturbations applied. In the axial direction (*z*, top panel) the 50 T seed magnetic field lowers perturbation growth due to magnetic tension stabilization [18, 20, 22]. However, in the azimuthal direction (*θ*, bottom panel) the perturbation growth is enhanced by magnetization, due to decreased thermal ablative stabilization [18]. The proposed experimental platform could be used to investigate the trade-off between these two effects for varying perturbation wavelengths.

is artificially modulated by $\pm 1\%$ sinusoidally in both θ and z. A mode 5 perturbation is used in θ, which matches the mode number of the baseline laser asymmetry [33]. In z a perturbation of 20 μm wavelength is applied.

The top panel in figure 4 shows the radially-integrated density (areal density) as a function of axial position at the time of peak neutron production, with and without a 50 T magnetic field applied. The average areal density is lower in the magnetized case, as the significant magnetic pressure decreases the compression. It can be seen that the size of the axial areal density perturbation is decreased with the magnetic field applied, as the magnetic tension stabilizes the perturbation [20].

In the azimuthal direction, however, the perturbation size is enhanced by magnetization (see bottom panel in figure 4).

In this orientation the magnetic tension does nothing to suppress the perturbation growth. Instead, suppression of electron thermal conduction decreases the stability, as thermal ablative stabilization is reduced; there is less ablation of cold plasma into the hot-spot to stabilize the growth [18]. This process is still occurring in the axial direction, but the magnetic tension stabilization dominates.

The effect of an applied magnetic field on the perturbation growth is a balance between the magnetic tension stabilizing axial perturbations and the decreased thermal ablative stabilization in all directions [18]. The balance between the two processes is highly dependent on magnetic field strength and the perturbation wavelength. Shorter wavelengths and higher field strengths are thought to be dominated by magnetic tension, while intermediate wavelengths and smaller magnetic fields are mostly affected by suppression of thermal conduction [18]. If an artificial perturbation is applied to these cylindrical implosions (for example through contouring of the shell) then these predictions could be tested experimentally, which would be of great benefit to the magnetized ICF community.

The significance of the magnetic tension stabilizing perturbations can be quantified by using linear magnetized Rayleigh-Taylor theory [20]. The minimum unstable length-scale due to the magnetic field alone (i.e. neglecting thermal conduction) can be written as:

$$\lambda_B = \frac{|B^2|}{\mu_0 (\rho_h - \rho_l) g},\tag{22}$$

where g is the acceleration of an unstable interface between a heavy and light fluids of densities ρ_h and ρ_l respectively. For a stagnating hot-spot the light fluid is the hot-spot density ρ, while the heavy fluid is the peak density ρ_{shell}. Again, by assuming frozen-in-flow, the minimum unstable wavelength due to magnetic tension can be written in terms of initial experiment conditions and stagnation quantities:

$$\lambda_B = \frac{\rho^2 B_0^2 \, t_{stag}}{\rho_0^2 \, \mu_0 (\rho_{shell} - \rho) V_{imp}}, \quad \text{if } \Gamma = 1.\tag{23}$$

All the key parameters for quantifying the relevance of different magnetized processes are summarized in table 1; namely, *(a)* Γ determines the effectiveness of magnetic flux compressing with the plasma, *(b)* Λ is a measure of how compressed the magnetic field becomes, *(c)* the magnetization of the electron orbits is captured by $\omega_e \tau_e$, *(d)* the importance of magnetic pressure to the plasma dynamics is characterized by β, *(e)* Π determines the significance of Ohmic dissipation, *(f)* L_{hs}/λ_B is the axial mode number above which magnetic tension stabilizes the hot-spot to linear Rayleigh-Taylor growth, *(g)* the twisting factor t_{stag}/t_{twist} determines whether the Hall term is expected to cause significant twists in the magnetic field profile, and finally, *(h)* Ξ then determines if thermal or current-driven transport is more important.

Magnetic fields are also predicted to result in deviations from Rutherford scattering, modifying the electron-ion Coulomb logarithm [84]. This effect is important once the electron Larmor radius is shorter than the plasma Debye length. Even

in the low density hot-spots that result from magnetized cylindrical implosions, this effect is calculated to be negligible, with the Larmor radius remaining 100 times larger than the Debye length in the most extreme cases simulated.

5. Magnetization regimes in cylindrical implosions

In this section, modifications to the nominal experiment are explored through the non-dimensional factors in table 1. It is shown that the metrics can be used to design implosions for different regimes where certain processes dominate magnetic flux compression, thermal transport and bulk hydrodynamics.

Throughout this section, metrics are taken as their definition and do not utilize the frozen-in-flow ($\Gamma = 1$) approximation. The 2D simulations are reduced to 0D metrics by taking the burn-averaged values.

First, the topic of magnetic flux compression is explored. Figure 5 plots Γ for a series of 2D simulations with various fill densities and applied field strengths. Note that varying the fuel density is used to modify the stagnation conditions, with all densities quoted as a multiple of the nominal deuterium fill density of 1.81 kg m^{-3}. While higher densities may not be practical from a target fabrication standpoint, lowering the fill density increases the implosion convergence ratio to an extent that is difficult to resolve with current simulations. Increased convergence may also be undesirable for the onset of hydrodynamic instabilities. Higher fill densities could be achieved by using a foam fuel instead. However, the current study keeps the fill composition as D_2 in order to differentiate the impact of changing ionization state from changing fill density. The calculation of Γ uses the burn-averaged density and magnetic field strength.

As shown in figure 5, low applied field strengths result in the flux compression being far below the frozen-in-flow approximation. This is primarily due to the Nernst term, which transports magnetic field in the same direction as the electron heat-flow. Like the heat-flow, the Nernst term is suppressed at higher magnetizations. The lower fill density cases have larger contributions from Nernst, which is due to a combination of the hot-spot being hotter and having a smaller radius, both amplifying the temperature gradients.

For higher applied fields, the Nernst term is almost completely suppressed. At 50 T, $\Gamma > 1$ for all fill densities simulated, meaning that the magnetic field has compressed more than the plasma itself. At first this seems counter-intuitive, as Nernst moves magnetic field out of the hot-spot and resistive diffusion acts to lower the field strength. However, here it is actually found that resistive diffusion can increase the field strength in the hot-spot and that axial motion allows for additional magnetic flux compression, as explained hereafter. It is important to remember that the compressed field and density values used to calculate Γ plotted in figure 5 are burn-averaged quantities, which means they sample the hot core at the centre more than the hot-spot edge. However, the hot-spot is lower density than the core periphery, meaning that the compressed field in the former is lower than in the surrounding plasma. Therefore, resistive diffusion acts to move magnetic flux from

Table 1. Non-dimensional numbers determining the relative importance of different physical processes in magnetized cylindrical implosions. These factors can be used to optimize an experiment to explore specific phenomena (see section 5) or can be inferred by using the frozen-in-flow approximation along with spectroscopy (see section 6).

Description	Symbol	Definition	$\Gamma = 1$ approximation
Frozen-in-flow factor	Γ	$\dfrac{\lvert\underline{B}\rvert}{B_0}\dfrac{\rho_0}{\rho}$	1
Field compression factor	Λ	$\dfrac{\lvert\underline{B}\rvert}{B_0}$	$\dfrac{\rho}{\rho_0}$
Electron Hall parameter	$\omega_e\tau_e$	$\propto \dfrac{\lvert\underline{B}\rvert T_e^{3/2}}{n_e}$	$\propto \dfrac{B_0}{\rho_0} T_e^{3/2}$
Ratio of thermal to magnetic pressure	β	$\dfrac{2(P_e+P_i)\mu_0}{\lvert\underline{B}\rvert^2}$	$\dfrac{2(1+Z)\rho_0^2\,T_e\mu_0}{m_i B_0^2\,\rho}$
Ohmic dissipation factor	Π	$\dfrac{t_{\text{stag}}}{t_{\text{diff}}}\dfrac{1}{\beta}$	$\dfrac{B_0}{\rho_0^3}\dfrac{t_{\text{stag}}\rho}{\tau_{ei}T_e}\alpha_\perp^c\dfrac{m_i^2\,m_e Z}{2(Z+1)e}$
Maximum unstable magnetic tension mode	L_{hs}/λ_B	$\dfrac{\mu_0(\rho_h-\rho_l)gL_{hs}}{\lvert B^2\rvert}$	$\dfrac{L_{hs}\rho_0^2}{\rho^2 B_0^2}\dfrac{\mu_0(\rho_{\text{shell}}-\rho)V_{\text{imp}}}{t_{\text{stag}}}$
Twisting factor	$t_{\text{stag}}/t_{\text{twist}}$	$\dfrac{2\lvert j\rvert t_{\text{stag}}}{L_{hs}en_e}$	$\dfrac{2}{L_{hs}}\dfrac{B_0}{R_0}\dfrac{\rho^{1/2}}{\rho_0^{3/2}}\dfrac{m_i}{\mu_0 Ze}$
Ratio of thermal to current-driven transport	Ξ	$\dfrac{\gamma_\perp^c\tau_{ei}T_e en_e\mu_0}{\lvert\underline{B}\rvert m_e}$	$\dfrac{\gamma_\perp^c\tau_{ei}T_e e\mu_0}{m_i m_e B_0}\dfrac{\rho_0 Z}{}$
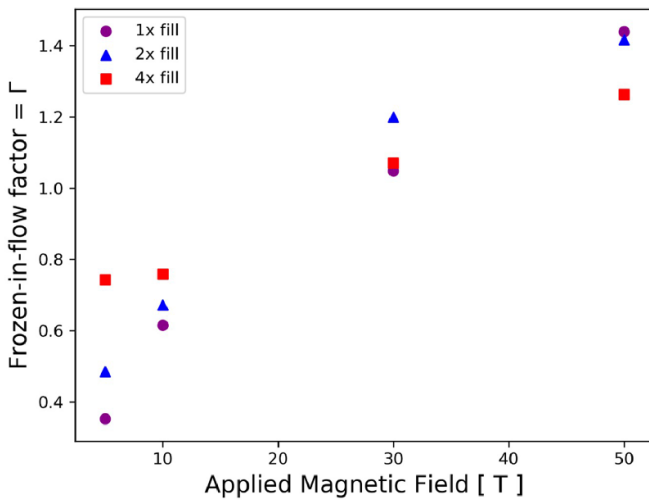
Figure 5. The frozen-in-flow factor $\Gamma = \lvert\underline{B}\rvert\rho_0/B_0\,\rho$ for 2D simulations over a range of applied magnetic field strengths and initial gas fill pressures. $\Gamma = 1$ means that the magnetic flux has perfectly compressed with the plasma density. Low applied field strengths result in extra Nernst de-magnetization of the hotspot. $\Gamma > 1$ can be obtained due to 2D motion reducing the plasma compression while the magnetic flux continues to compress.

the compressed low temperature fuel to the low density hot-spot, increasing the plasma magnetization in the process.

The axial plasma motion also enhances the magnetic flux compression. As this is a cylindrical implosion, there are significant end losses out of the hot-spot [33]. These unconfined hot-spots can be compressed to a smaller radius. While the axial motion removes mass from the hot-spot, it does not remove magnetic flux, which is predominantly axial itself. Therefore, more axial motion of plasma allows higher

compression of the magnetic field. In theory, the greatest magnetic flux compression can be reached by driving extreme axial flows. If the aim of the experiment is to reach large electron magnetizations, however, large axial flows result in lower hot-spot temperatures and low burn durations. The low fill 50 T simulation has the largest Γ of greater than 1.4, as the axial flows driven are larger than the higher fill densities.

Note that $\Gamma < 1$ is always expected in experiments where the fuel is laser preheated, such as MagLIF [28]. The fuel becomes hot even before the magnetic flux is compressed, resulting in low electron magnetizations and large temperature gradients, allowing Nernst demagnetization to dominate.

Mid- or high-Z dopant mixed into the capsule fuel helps to increase magnetic field compression. In particular, figure 6 plots the compression factor Λ as a function of argon concentration—the percentage quoted is per deuterium atom—for 2D simulations with 5, 30 and 50 T applied fields. While applying a 50 T field invariably results in higher compressed field strengths than a 30 T field, the compression factor is always lower. This is because the higher applied field strengths result in lower hot-spot compression. The reasons for this are twofold. Firstly, suppression of thermal conduction reduces the hot-spot compressibility, increasing the temperature at the cost of the density (giving the same stagnated pressure) [62]. Secondly, the final total pressure is the same; higher magnetic pressure results in a lower thermal pressure [33].

For the 5 T case in figure 6, increasing the dopant concentration greatly increases the magnetic flux compression. This is because the hot-spot radiatively cools, reducing the thermal pressure and allowing for more compression. The same is true in principle for the 50 T case. However, the hot-spot deceleration is not just dominated by the thermal pressure when 50 T is applied, since the magnetic pressure is significant—as will be seen later in figure 8(a), the ratio of thermal to magnetic
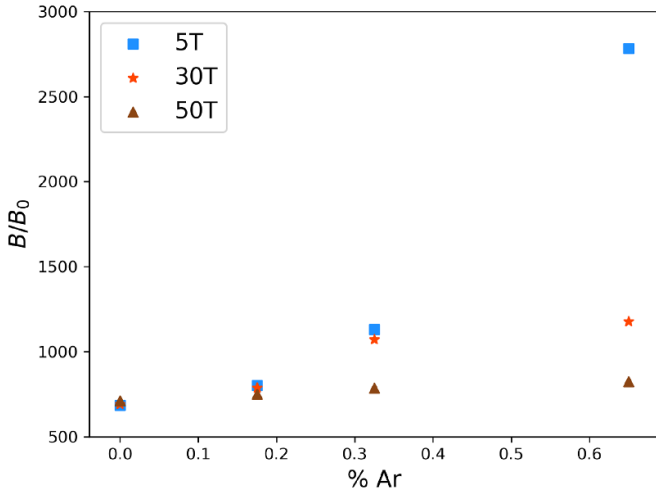
Figure 6. Burn-averaged field compression factor $\Lambda = |\underline{B}|/B_0$ for 2D simulations over a range of argon dopant concentrations and with applied magnetic fields of 5, 30 and 50 T. Lower applied field strengths are easier to compress, as electron heat-flow magnetization results in a high temperature, low density hot-spot. In addition, large magnetic pressures result in lower compression. Introducing a dopant to the fuel increases magnetic field compression. For a large initial field strength, the magnetic pressure sets the magnetic field compression (rather than the plasma thermal pressure), reducing the compression factor dependence on dopant concentration.

Figure 7. Burn averaged electron and ion temperatures for 2D simulations for a range of gas fill pressures and applied field strengths. Larger magnetic fields reduce the electron thermal conduction losses from the hot-spot, raising the temperature. Higher fill pressures result in lower plasma magnetizations, reducing the temperature enhancement. In the regime of large magnetic pressure, the electron temperature can exceed the ion temperature due to Ohmic dissipation.

pressure is ~ 1. Therefore, the dopant has less of an impact on the magnetic field compression and leads to the magnetic field compression factor being relatively independent of the dopant concentration, as seen in figure 6.

Figure 7 shows the burn-averaged electron and ion temperatures of 2D simulations scanning both applied field strength and fill density. For these cases, a dopant concentration of 0.325% is used. As the magnetic field strength is increased, the thermal conduction from the hot-spot into the cold fuel is suppressed, raising the core temperature. For the 50 T low fill density case the electron Hall parameter reaches a burn-averaged value of over 300, reducing the thermal conductivity perpendicular to the magnetic field to $\kappa_\perp/\kappa_\parallel = 5 \times 10^{-5}$.

The higher fill densities reach lower temperatures, reducing the electron magnetization. Therefore, the enhancement in temperature is lower for a higher initial fill density.

An interesting feature in figure 7 is the electron temperature being larger than the ion temperature in the highly magnetized low fill density cases. This is due to the Ohmic dissipation converting magnetic energy into electron thermal energy. In unmagnetized implosions the electron population loses energy faster than the ions due to their additional mobility. Typically it is through electron-ion collisions that the ion population loses its energy, but in the magnetized case a significant proportion of the implosion kinetic energy is used to compress the magnetic field ($\beta \approx 1$). Once the field starts to diffuse and relax, this potential energy is transferred to the electrons, which are resistively heated. For $B_0 = 50$ T, the Ohmic heating factor is $\Pi = 0.13$ at the hot-spot edge, indicating that a significant proportion of the magnetic energy is being transferred into electron thermal energy.
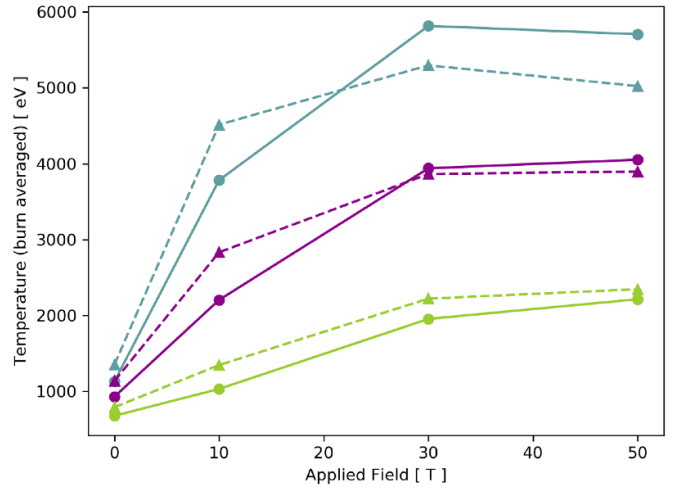
Measuring a higher electron temperature than ion temperature would be a definitive observation of this process taking place. However, there may be complications due to the ion temperature typically being inferred by the spectra of fusion-produced neutrons [72]. Doppler shifting of the spectra by fluid motion can increase the apparent ion temperature, which may be comparable in size to the ≈ 500 eV difference in electron and ion temperatures reported here.

Figure 8(b) displays the dependence of a range of metrics from table 1 on the applied field strength. Universally, these all show the importance of the induced current increasing with applied field strength. For an applied field of 50 T the hot-spot magnetic pressure is approximately the same size as the thermal pressure, giving a $\beta \approx 1$. Along with this, the axial mode numbers that are suppressed by magnetic tension (L_{hs}/λ_B) decreases to 12, meaning that all high mode features are expected to be suppressed in the axial direction. The importance of thermal transport of magnetic field and electron energy is almost completely suppressed by electron magnetization, which can be seen from $\Xi < 0.001$. While the magnetic field twisting factor is still small for a seed B-field of 50 T, this could be enhanced by reducing the driving length of the target.

Figure 8(b) then shows how the induced-current metrics vary with the argon dopant percentage for an applied magnetic field of 30 T. Again, the added dopant results in additional radiative losses, allowing the hot-spot to become more compressed. Similarly, the magnetic field compresses further and gives larger induced currents. As a result, the magnetic pressure is greater, the Ohmic heating becomes more important, the magnetic tension stabilizes more wavelengths, the importance of thermal transport is reduced and the Hall term twists the magnetic field more effectively.
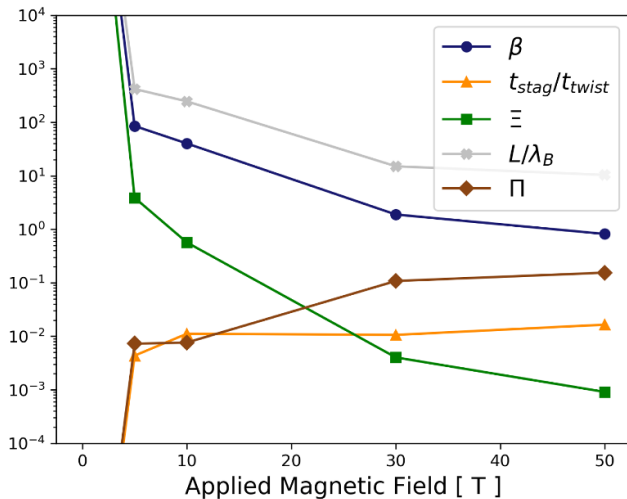
(a)
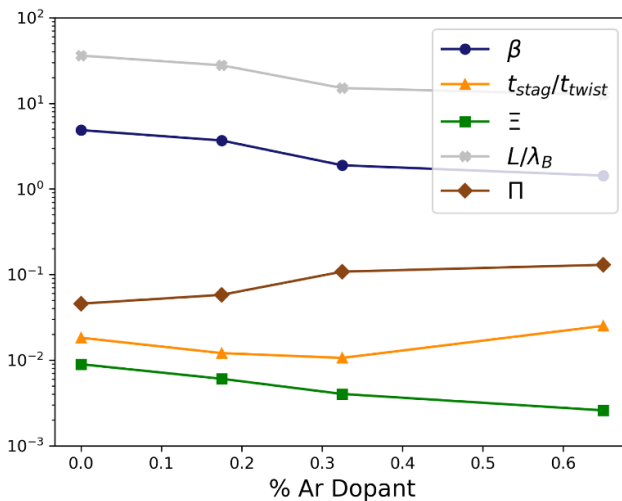
(b)

Figure 8. Magnetization metrics from table 1 for: (a) varying the applied field strength while keeping the argon concentration at 0.325% by atom; (b) varying the argon fuel dopant concentration while keeping the applied field strength at 30 T.

6. Argon K-shell spectroscopy

Here we address the application of x-ray spectroscopy for the characterization of core conditions. The Gorgon MHD simulations show that the compression of the B-field changes the hydrodynamic behaviour, thus producing a variety of magnetization phenomena whose underlying physics demand a deeper understanding as discussed in sections 4 and 5. Since changes in the hydrodynamics translate into significant variations in the radial profiles of core temperature and density throughout the implosion collapse compared to the unmagnetized case, a way to bring information about the associated physics is by diagnosing the conditions of the imploding core. In this regard, given the success in past experimental

campaigns of spherical implosions at OMEGA [42–46] and also in laser-heated cylindrical plasma experiments performed at Z related to the MagLIF preheat stage [47, 48], here we propose to rely on time-resolved Ar K-shell spectroscopy. This diagnostic exploits two basic properties of the Ar K-shell spectrum emitted from hot, dense plasmas: (1) the Stark-broadened line shapes strongly depend on density and are relatively insensitive to variations in electron temperature, (2) the relative intensity distribution of K-shell lines and their associated satellites are sensitive to variations in electron temperature and density through the dependence to these parameters on the atomic level population kinetics. The Ar K-shell spectroscopic technique works properly for plasma electron densities and temperatures typically in the ranges of $n_e \sim 10^{23} - 10^{24}$ cm^{-3} and $T_e \sim 600$–2000 eV, since for these conditions the Stark effect is the dominant line broadening mechanism, and He-like and H-like Ar are significantly populated so that their corresponding line emission becomes bright and useful for analysis. In this regard, figure 9 shows the time histories of mass-weighted average electron temperature and electron density of the imploded core for different argon concentrations obtained from 2D Gorgon simulations. Overall, average core conditions for the non-magnetized implosions fit well within the ranges above, while for the magnetized case the temperature can go above 2 keV around stagnation. Still, since the new physics and main goal here focuses on exploring and providing evidence on extreme magnetization phenomena, we consider appropriate to use the well-established Ar K-shell spectroscopic technique and perform an assessment of its potential application, in order to find out how far the technique can be pushed for the characterization of core conditions in the magnetized scenario. It is also worth noting that despite the high B-field values achieved in the compressed core (>10 kT around stagnation), Stark-Zeeman spectroscopy cannot be used to obtain an estimation of compressed B-field in an experimental scenario. Given the range of electron densities achieved, we performed systematic calculations of Stark-Zeeman line profiles based on molecular dynamics simulations [73] and checked that the broadening of Ar K-shell lines produced by the Stark effect blurs the characteristic Zeeman pattern even in the case of the expected achievable B-field. Zeeman features will be further washed out by radiation transport effects through the imploded core and instrumental broadening. Details of these calculations are beyond of the scope of this paper and will be addressed in a forthcoming publication.

In an effort to have a realistic representation of the time-resolved Ar K-shell spectra to be measured in a real experiment, we have post-processed the 2D MHD Gorgon simulations and performed detailed atomic-kinetics and radiation transport calculations throughout the evolution of the imploding cylinder. Line of sight is assumed to be perpendicular to the cylinder axis, so that to compute the emergent intensity the radiation transport equation must be solved along chords inside the plasma source parallel to the line of sight. The solution to this problem can be well approximated by a system of effective slabs [74] resulting from the discretization of the cylindrical plasma in a finite number of
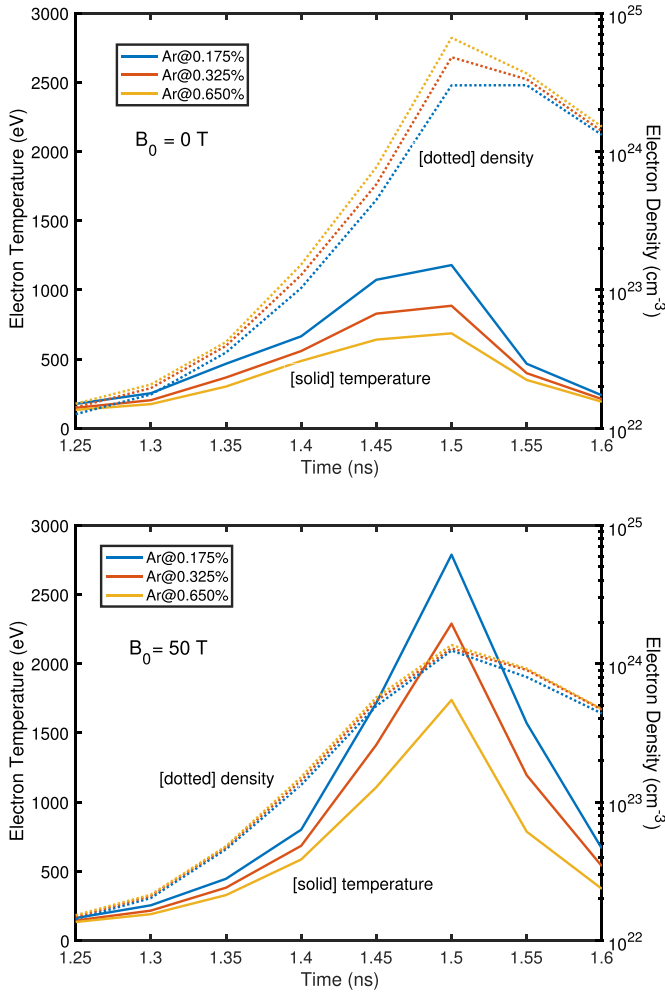
Figure 9. Time history of core conditions from 2D Gorgon simulations of cylindrical implosions as a function of different argon dopant concentrations. Shown values are obtained as mass-weighted averages within the radial core boundary and over the central 400 μm-long portion of the imploded cylinder. Top and bottom panels show electron temperature and electron density from non-magnetized and magnetized cases, respectively.

cylindrical shells, which here was chosen to exactly match the radial grid used in the Gorgon MHD simulations. Temperature and density conditions of each cylindrical shell are taken as the spatial average for a given time over the central 400 μm-long portion of the imploded core along the axial direction. This is a reasonable simplification, since according to MHD simulations—see figure 2—conditions of the imploded cylinder show little dependence on the axial direction in the central region. The required emissivities, opacities and atomic level population distributions were calculated with the collisional-radiative model ABAKO [75] for each pair of core electron temperature and density over the corresponding radial grid as obtained from the Gorgon MHD output, i.e. no interpolation over pre-calculated emissivity and opacity databases was applied. Bound-bound, bound-free and free-free contributions from the Ar-doped deuterium plasma within the spectral range of interest were included. In particular, relevant bound-free cross sections [76] were computed

with the LANL suite of codes [77]. Energy levels and line transitions rates for the required Ar ion stages were computed with the atomic structure code FAC [78]. For given plasma conditions, ABAKO explicitly includes all non-autoionizing and autoionizing states consistent with the corresponding ionization potential depression, which is estimated according to the Stewart-Pyatt model [79], modified to account for the argon-deuterium mixture. An escape factor model was used to account for radiation trapping effects on the atomic-level population kinetics [80]. Importantly for this application, detailed Stark-broadened line shapes for Ar Heα, Heβ, Heγ, Lyα, Lyβ, and Lyγ, and associated satellites were calculated with the MERL line-shape code [81], including ion-dynamics effects [82]. Recently, MERL Stark-broadened line shapes of Ar K-shell have been further validated for spectroscopic diagnosis applications against full molecular dynamics simulations [83].

Figure 10 shows the time evolution of the computed Ar K-shell emission, i.e. synthetic *streaked* images, for unmagnetized and magnetized cases assuming a seed B-field of 50 T. Besides Doppler and Stark broadening mechanisms, synthetic spectra also accounts for instrumental broadening. Consistently with available streaked spectrometers on OMEGA for the photon energy range of interest, a spectral resolution of $E/\Delta E \approx 500$ was assumed. Main line transitions in He-like and H-like ions are labelled, i.e. Heα (1s2p$\rightarrow$1 s^2), Heβ (1s3p$\rightarrow$1 s^2) and Heγ (1s4p$\rightarrow$1 s^2) in He-like Ar, and Lyα (2p$\rightarrow$1 s), Lyβ (3p$\rightarrow$1 s) and Lyγ (4p$\rightarrow$1 s) in H-like Ar. There are significant differences between the expected time-resolved spectra of a non-magnetized implosion and a magnetized one. Moreover, the metrics analysis of section 5 demonstrated that a extreme magnetization regime is already attainable for a seed B-field of 30 T, thus also expecting noticeable differences—similar to those shown in figure 10—in the spectral output when compared to the unmagnetized case. Therefore, based on our simulations, in a potential experimental realization the observation of the time-resolved Ar K-shell emission should be able to distinguish between the unmagnetized and magnetized scenarios (at least for $B_0 > 30$ T). A detailed analysis of spectroscopic data would bring further information about the magnetization state, as pointed out below.

For interpretation, it is useful to correlate the synthetic streaked images in figure 10 with the time histories of electron temperature and density shown in figure 9. In the unmagnetized case, line emission turns on at $t \gtrsim 1.35$ ns and lasts for $\lesssim 200$ ps. Figure 10 shows that, overall, as expected, signal intensity increases with time until stagnation ($t = 1.5$ ns), when the average temperature and density reach their maximum values, and decreases after. Lines are narrower early in time, then gradually broaden until stagnation time and narrowing down afterwards, mainly due to Stark-broadening which increases with increasing electron density. When comparing the results for different Ar concentrations, the ratio of He-like to H-like for the same type of transition increases with the Ar amount. This is a result of radiative cooling, i.e. core temperature decreases and He-like ion population is favoured relative to that of H-like ion. Also, core compressibility is higher for the case of Ar at 0.65%, so we observe broader
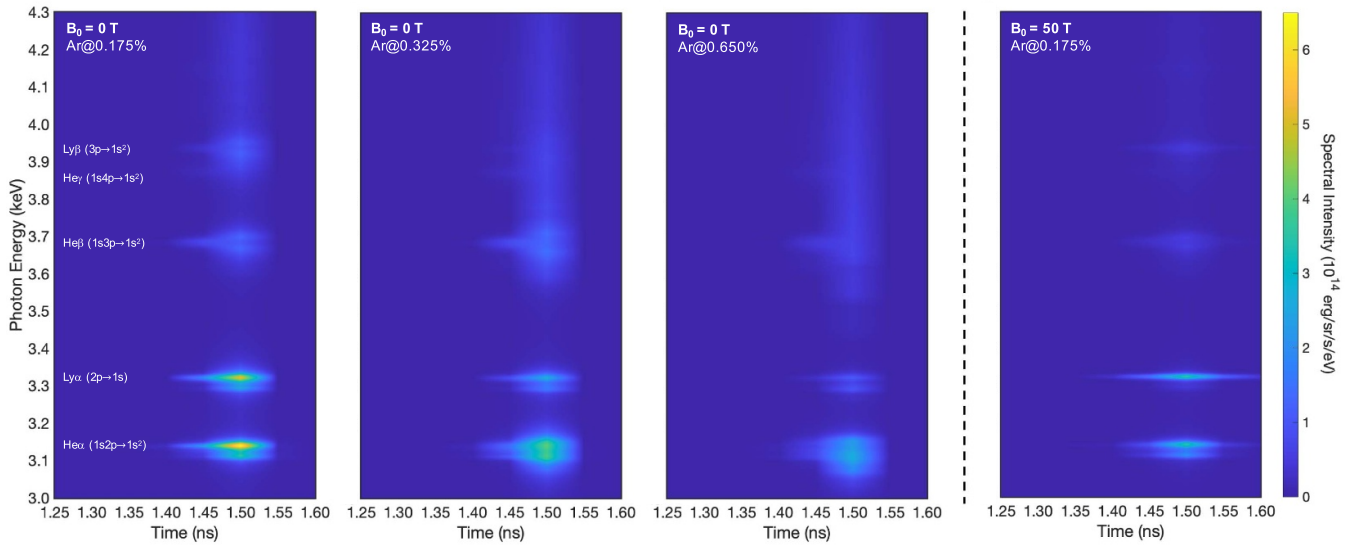
Figure 10. Comparison of synthetic images of Ar K-shell time-resolved spectra for unmagnetized and magnetized ($B_0 = 50$ T) implosions. For the non-magnetized case, changes in the spectra due to different Ar concentrations are shown. For the magnetized case, the sensitivity with Ar concentration is lost and only the case for Ar at 0.175% is displayed—see the text for details.

lines when compared to the results for Ar at 0.175%. For Ar at 0.65% the overall spectral intensity drops compared to Ar at 0.175%, which, despite the density increasing, can be explained because the plasma cooling remains as the dominant effect; i.e. for Ar at 0.65%, the core average temperature stays below 700 eV throughout the implosion and, relative to the case of Ar at 0.175%, the ion population distribution shifts to lower ionization stages, so that the number of K-shell ion emitters decreases accordingly.

In the magnetized case, line emission lasts longer ($\sim$250 ps) and the overall signal intensity is lower than compared to a non-magnetized implosion. Moreover, since the effect of magnetic pressure reduces the core compressibility, electron density and therefore the impact of Stark-broadening decrease, which ultimately leads to narrower lines compared to the unmagnetized scenario. Interestingly, contrary to what was found for unmagnetized implosions, streaked images of K-shell emission show little sensitivity to the Ar concentration—only the case for Ar at 0.175% is displayed in figure 10 due to this reason. This is due to the large gradients in core conditions along the radial direction throughout the collapse of the implosion for the magnetized case. For illustration, figure 11 shows the radial profiles at stagnation time of core electron temperature and density averaged in the axial direction over the central 400 μm-portion of the imploding cylinder. Figure 11(a) shows the case without a magnetic field and figure 11(b) shows the case with a 50 T applied field. The temperature radial profiles show that, regardless of the Ar amount, a lower bound of $\sim$700 eV is found at the core periphery. Temperature rises radially inwards to values far above $\sim$2 keV for 50 T, where Ar ions will be fully ionized. Thus, it is clear that K-shell emission for the magnetized case will be only representative of the core outermost portion. When temperature spatial profiles are correlated with the corresponding density profiles, one realizes that, no matter the Ar concentration, the radiation

transport comes across basically the same ranges and combinations of core conditions relevant for K-shell line emission. Accordingly, since a similar behaviour is found over the implosion collapse, the resulting time-resolved spectra show little dependence on the Ar amount. No significant gradients are observed in the radial profiles for the unmagnetized case. In section 5, the variation of Ar concentration was suggested as a fine-tuning knob for achieving different magnetization regimes for a given seed B-field value. However, since the sensitivity with Ar concentration is lost, our simulations here show that Ar K-shell spectroscopy would not be useful to distinguish between such regimes. Still, if ideally multiple spectrometers were available in the experimental facility to simultaneously measure different spectral ranges, we could keep using the dopant concentration as a control knob and speculate with doping the targets with small amounts of different dopants, for instance mixing Ar and Kr. Ar K-shell spectroscopy seems to work properly for the characterization of core conditions in the unmagnetized case and, potentially, Kr K-shell and L-shell spectroscopy could provide a better characterization of magnetized implosions, even enabling to retrieve the sensitivity of the emission spectra to the dopant concentration. This subject is under investigation and will be published elsewhere.

Figure 12 shows synthetic time-integrated spectra for the unmagnetized and magnetized cases to evaluate potential data from this diagnostic on OMEGA. Spectra are shown for a photon energy from 3500 to 4300 eV, since temperature and density diagnosis based on K-shell spectroscopy usually relies on the β and γ lines region of the spectrum—α lines are much more sensitive to spatial gradients and absorption effects than others due to their characteristic large optical depths–. As already discussed, there is little variation with Ar concentration for the magnetized case, so that only the case for Ar at 0.175% is displayed. The comparison of time-integrated
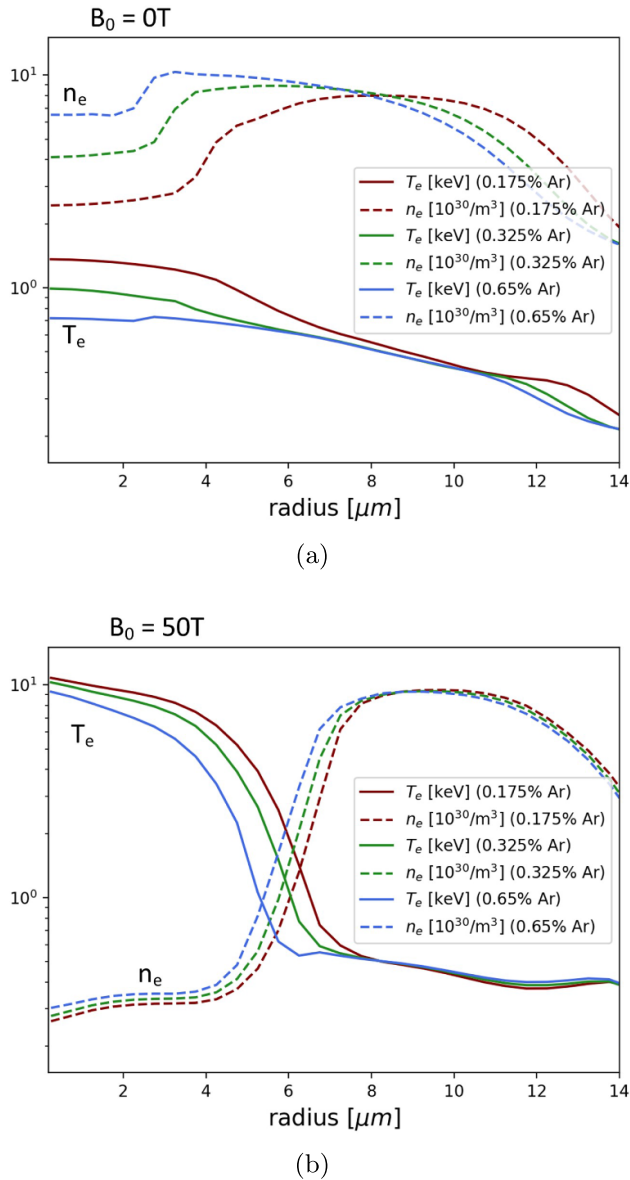
(a)

(b)

Figure 11. Radial profiles of core conditions at stagnation time ($t = 1.5$ ns) for a magnetized cylindrical implosion with $B_0 = 0$ T (top) and $B_0 = 50$ T (bottom). Results for different Ar concentrations are shown. The magnetized case has much larger gradients between the hot-spot core and the shell.
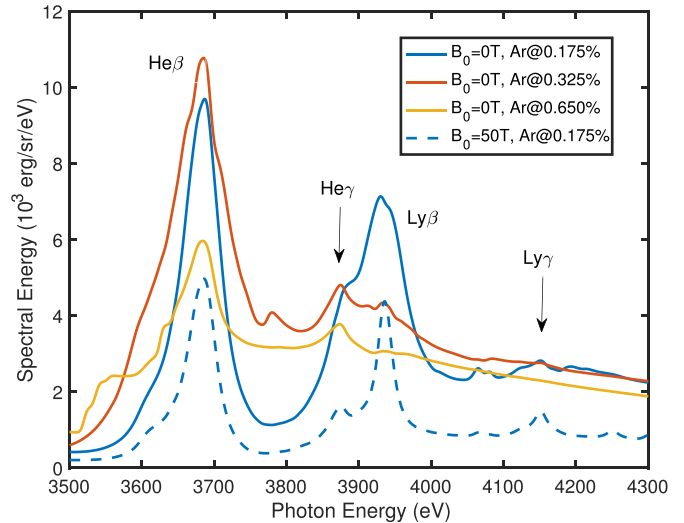

Figure 12. Comparison of synthetic Ar K-shell time-integrated spectra for non-magnetized and magnetized ($B_0 = 50$ T) implosions. For the unmagnetized case, changes in the spectrum due to different Ar concentrations are shown. For the magnetized case, the sensitivity with Ar concentration is lost and only the case for Ar at 0.175% is displayed—see the text for details.

results for non-magnetized and magnetized implosions differ in a factor of ~ 2, and both compare within one order of magnitude with calculations done in the past for the campaign of spherical implosions on OMEGA, where the Ar K-shell emission was successfully recorded. Therefore, for all the reasons above, an argon concentration of 0.175% seems to be a good choice for application of K-shell spectroscopy for the study of the referred direct-drive cylindrical implosions.

Lastly, it is worth noting that, similarly to previous work, a spectroscopic modelling and analysis of the measured time-resolved Ar K-shell emission would allow the determination of the temperature and density of the imploded core throughout the collapse of the implosion. From these spectroscopic measurements and if the magnetic field is assumed to be frozen, estimations for the magnetization metrics in table 1 can be obtained. However, in the magnetized scenario, the spectroscopic diagnosis will be more complicated due to the severe gradients in core conditions. A feasibility assessment of the spectroscopic technique based on synthetic data is on progress and will be published in a forthcoming paper.

7. Conclusions

This paper outlines a cylindrical implosion platform for studying highly magnetized plasmas on the OMEGA laser facility. In the highly magnetized regime the imploding shell decelerates on the magnetic field, converting kinetic energy into magnetic. The highly compressed magnetic field induces large electrical currents in the hot-spot; finite plasma resistivity results in Ohmic dissipation, diffusing the magnetic field and heating the electron population. This is expected to result in a higher temperature in the electron population than in the ions, which may be diagnosable.

spectra obtained at different Ar concentrations for a non-magnetized implosion allows us to answer the question about the optimum dopant concentration for spectroscopic purposes. For Ar at 0.175%, strong Heβ and Lyβ emissions are observed, which is critical for a reliable spectroscopic analysis. For Ar at 0.325% the Lyβ emission is almost lost and the situation is even worse for Ar at 0.650%. The same conclusion is found when doing the comparison for time-resolved spectra. Besides the difference in the absolute signal strength, time-integrated spectra from unmagnetized and magnetized cases mostly differ in the broadening of the lines. The higher compressibility of the unmagnetized implosion ultimately leads to a significant impact of Stark-broadening, which is not so severe in the magnetized case. Regarding the overall signal strength,

The large induced electrical currents can also cause Hall physics to be important, which has not been reported in laser-driven implosions to date. The calculations here estimate that a typical electron in the hot-spot will undergo a 1/3 rotational drift around the cylindrical axis within the fusion time frame, advecting the magnetic field and electron energy distribution.

The electrical currents also result in perturbation stabilization in the axial direction, which could be studied by using a shell with applied corrugations. Experiments scanning applied field strength and perturbation wavelength would be of great interest to the magnetized ICF community.

All of these magnetization processes have been summarized as non-dimensional metrics in table 1.

Care has been taken to optimize future potential experiments to reach peak magnetic field strengths. By using a low gas fill, the magnetic field is more easily compressed. However, as the convergence ratio of the capsule increases, the implosion will be more susceptible to perturbation growth, limiting the minimum fill density. Dopants added to the imploding fuel can also be used to radiatively cool the hot-spot, allowing the magnetic field to be more compressible. More axial motion, too, allows for greater flux compression.

X-ray spectroscopy can be used to diagnose the core electron temperature and density. The core temperature is anticipated to increase through the application of a magnetic field, while the density will decrease. The measurement of lower overall core pressure when a large magnetic field is applied would indicate that the magnetic pressure has become significant. By assuming frozen-in-flow, which has been shown with simulations to be a good approximation in the highly magnetized regime, many of the metrics governing which magnetization phenomena are important can be indirectly inferred.

Data availability statement

The data generated and/or analysed during the current study are not publicly available for legal/ethical reasons but are available from the corresponding author on reasonable request.

Acknowledgments

Appendix

Magnetic flux compression has been measured in previous cylindrical implosions on the OMEGA Laser Facility using proton radiography [5, 6]. Here, 2D Gorgon simulations are post-processed to create synthetic proton radiographs to compare with these experiments. Good agreement is found when the Nernst term is included in the simulations. These results build confidence in the simulation results in this publication and also (to a lesser extent) in other non-cylindrical Gorgon simulations where magnetic flux compression is an important process.

There are significant differences between the target dimensions used in the bulk of this paper and the target used for this magnetic flux compression validation. Here the target radius is $430\,\mu$m, filled with 3 atm of D_2 gas [6]. A 5 T magnetic field was applied, which is low enough to have relatively little contribution from magnetic pressure in the hot-spot. The experiment discussed in this appendix was also carried out before the laser non-uniformity was optimized [31, 60], resulting in a lack of axial hot-spot confinement. While this lowers the electron magnetization, the Gorgon simulations actually predict an enhancement to the magnetic flux compression, because the hot-spot is more compressible.

The proton source in the experiment was from an exploding pusher, which provides a relatively monoenergetic proton population ($\Delta E/E \sim 0.03$) [6]. This population is born at 14.7 MeV, but is accelerated to 15.2 MeV due to charging
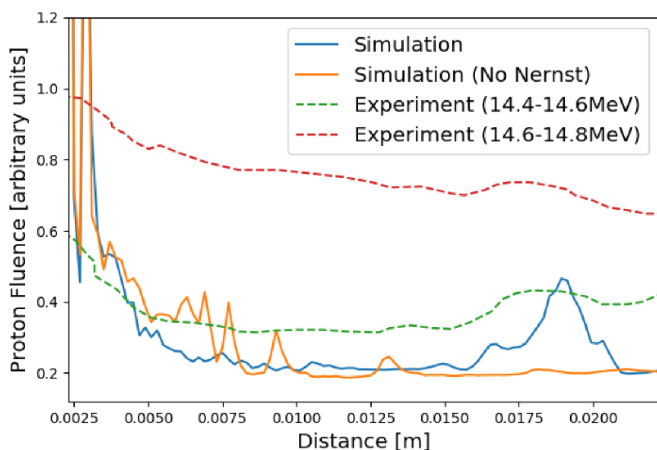
Figure A1. Proton radiographs of a cylindrical magnetic flux compression experiment. The experimental data is taken from [6], showing here only the data from the protons that have slowed through the target (energy ranges 14.4–14.6 MeV and 14.6–14.8 MeV). The experimental radiographs show a bump at around 1.8 cm, which is consistent with the simulation including Nernst advection.

of the backlighter [6]. The hot-spot being imaged is small ($\approx 10\,\mu$m), meaning that very few protons hitting the radiograph are significantly deflected by the compressed magnetic field. On the face of it, this makes imaging the peak field very difficult. However, the protons passing through the compressed plasma are slowed; by looking only at the protons that have had their energies lowered by the compressed plasma, the signal to noise ratio is improved. In the experiment analysis, the proton populations in the energy bands $< 14.4, 14.4$–14.6 and 14.6–14.8 MeV all show bumps at around 1.8 cm deflection [6]. When the applied field was reversed in direction, the bump moved to -1.8 cm, which indicates that the feature is from magnetic field deflections, not from electric field effects. While the signals for each proton range are relatively small compared with the background, the consistency of the feature across several proton energy ranges and across multiple experiments is encouraging.

Synthetic proton radiographs of 2D Gorgon simulations have been plotted in figure A1. These are produced using a proton tracking code without electric field effects or collisional scattering. A monoenergetic source is assumed. The protons are reported to be emitted over a 150 ps burst [6], so a Gaussian emission profile with standard deviation of 75 ps is used for the synthetic radiographs.

When the Nernst term is included in the simulations a bump is observed in the radiograph at 1.9 cm, similar to that seen experimentally. This bump is not found to be due to the peak field strength reached at the centre of the target, but by the magnetic flux that develops at the hot-spot edge, $\approx 10\,\mu$m from the axis. While the field strength at this radius is lower, deflecting the protons less, the total flux of protons into this region is greater, increasing the signal. The magnetic field strength at the hot-spot edge is approximately 4000 T, which is consistent with the values inferred by the original experiment analysis [5].

Without the Nernst term included, the synthetic proton radiograph does not compare favourably with the experiment, with a wide spread of proton deflections and no clear bump— see figure A1. This is the first direct evidence of Nernst in magnetized implosions; Nernst has been indirectly inferred in MagLIF through observation that, above a certain laser preheat energy, the neutron yield plateaus [28]. No sensitivity of the radiograph to a Nernst flux limiter in the range 0.04–0.1 was found. While resistive diffusion smooths the radiograph, the cases with and without compare equally favourably to the experiment.

ORCID iDs

C A Walsh ⓘ https://orcid.org/0000-0002-6639-3543
R Florido ⓘ https://orcid.org/0000-0001-7428-6273
M Bailly-Grandvaux ⓘ https://orcid.org/0000-0001-7529-4013
G Pérez-Callejo ⓘ https://orcid.org/0000-0003-3719-2352
C Vlachos ⓘ https://orcid.org/0000-0003-4834-1536
F N Beg ⓘ https://orcid.org/0000-0003-0391-8944
J J Santos ⓘ https://orcid.org/0000-0002-4737-8559

References

[1] Lai D 2001 Matter in strong magnetic fields *Rev. Mod. Phys.* **73** 629
[2] Engel D and Wunner G 2008 Hartree-Fock-Roothaan calculations for many-electron atoms and ions in neutron-star magnetic fields *Phys. Rev.* A **78** 032515
[3] Murdin B N *et al* 2013 Si:P as a laboratory analogue for hydrogen on high magnetic field white dwarf stars *Nat. Commun.* **4** 1469
[4] Hohenberger M, Chang P-Y, Fiksel G, Knauer J P, Betti R, Marshall F J, Meyerhofer D D, Sééguin F H and Petrasso R D 2012 Inertial confinement fusion implosions with imposed magnetic field compression using the OMEGA Laser *Phys. Plasmas* **19** 056306
[5] Gotchev O V *et al* 2009 Laser-driven magnetic-flux compression in high-energy-density plasmas *Phys. Rev. Lett.* **103** 215004
[6] Knauer J P *et al* 2010 Compressing magnetic fields with high-energy lasers *Phys. Plasmas* **17** 056318
[7] Pollock B B *et al* 2006 High magnetic field generation for laser-plasma experiments *Rev. Sci. Instrum.* **77** 114703
[8] Albertazzi B *et al* 2013 Production of large volume, strongly magnetized laser-produced plasmas by use of pulsed external magnetic fields *Rev. Sci. Instrum.* **84** 043505
[9] Fiksel G *et al* 2015 Note: experimental platform for magnetized high-energy-density plasma studies at the omega laser facility *Rev. Sci. Instrum.* **86** 016105
[10] Fujioka S *et al* 2013 Kilotesla magnetic field due to a capacitor-coil target driven by high power laser *Sci. Rep.* **3** 1170
[11] Santos J J *et al* 2015 Laser-driven platform for generation and characterization of strong quasi-static magnetic fields *New J. Phys.* **17** 083051
[12] Law K F F *et al* 2016 Direct measurement of kilo-tesla level magnetic field generated with laser-driven capacitor-coil target by proton deflectometry *Appl. Phys. Lett.* **108** 091104
[13] Goyon C *et al* 2017 Ultrafast probing of magnetic field growth inside a laser-driven solenoid *Phys. Rev.* E **95** 033208

[14] Tikhonchuk V T, Bailly-Grandvaux M, Santos J J and Poyé A 2017 Quasistationary magnetic field generation with a laser-driven capacitor-coil assembly *Phys. Rev.* E **96** 023202

[15] Santos J J *et al* 2018 Laser-driven strong magnetostatic fields with applications to charged beam transport and magnetized high energy-density physics *Phys. Plasmas* **25** 056705

[16] Chang P Y, Fiksel G, Hohenberger M, Knauer J P, Betti R, Marshall F J, Meyerhofer D D, Seguin F H and Petrasso R D 2011 Fusion yield enhancement in magnetized laser-driven implosions *Phys. Rev. Lett.* **107** 035006

[17] Perkins L J, Ho D D-M, Logan B G, Zimmerman G B, Rhodes M A, Strozzi D J, Blackfield D T and Hawkins S A 2017 The potential of imposed magnetic fields for enhancing ignition probability and fusion energy yield in indirect-drive inertial confinement fusion *Phys. Plasmas* **24** 062708

[18] Walsh C A, Mcglinchey K, Tong J K, Appelbe B D, Crilly A, Zhang M and Chittenden J P 2019 Perturbation modifications by pre-magnetisation of inertial confinement fusion implosions *Phys. Plasmas* **26** 022701

[19] Sio H *et al* 2021 Diagnosing plasma magnetization in inertial confinement fusion implosions using secondary deuterium-tritium reactions *Rev. Sci. Instrum.* **92** 043543

[20] Chandrasekhar S and Gillis J 1962 Hydrodynamic and hydromagnetic stability *Phys. Today* **15** 58

[21] Sano T, Inoue T and Nishihara K 2013 Critical magnetic field strength for suppression of the Richtmyer-Meshkov instability in plasmas *Phys. Rev. Lett.* **111** 205001

[22] Srinivasan B and Tang X-Z 2013 The mitigating effect of magnetic fields on Rayleigh–Taylor unstable inertial confinement fusion plasmas *Phys. Plasmas* **20** 056307

[23] Walsh C, Crilly A and Chittenden J 2020a Magnetized directly-driven ICF capsules: increased instability growth from non-uniform laser drive *Nucl. Fusion* **60** 106006

[24] Slutz S A, Herrmann M C, Vesey R A, Sefkow A B, Sinars D B, Rovang D C, Peterson K J and Cuneo M E 2010 Pulsed-power-driven cylindrical liner implosions of laser preheated fuel magnetized with an axial field *Phys. Plasmas* **17** 056303

[25] Gomez M R *et al* 2014 Experimental demonstration of fusion-relevant conditions in magnetized liner inertial fusion *Phys. Rev. Lett.* **113** 155003

[26] Gomez M R *et al* 2015 Demonstration of thermonuclear conditions in magnetized liner inertial fusion experiments *Phys. Plasmas* **22** 056306

[27] Knapp P F *et al* 2015 Effects of magnetization on fusion product trapping and secondary neutron spectra *Phys. Plasmas* **22** 056312

[28] Gomez M R *et al* 2020 Performance scaling in magnetized liner inertial fusion experiments *Phys. Rev. Lett.* **125** 155002

[29] Davies J R, Barnak D H, Betti R, Campbell E M, Chang P-Y, Sefkow A B, Peterson K J, Sinars D B and Weis M R 2017 Laser-driven magnetized liner inertial fusion *Phys. Plasmas* **24** 062701

[30] Barnak D H *et al* 2017 Laser-driven magnetized liner inertial fusion on OMEGA *Phys. Plasmas* **24** 056310

[31] Hansen E C *et al* 2018 Optimization of laser-driven cylindrical implosions on the omega laser *Phys. Plasmas* **25** 122701

[32] Davies J R, Barnak D H, Betti R, Campbell E M, Glebov V Y, Hansen E C, Knauer J P, Peebles J L and Sefkow A B 2019 Inferring fuel areal density from secondary neutron yields in laser-driven magnetized liner inertial fusion *Phys. Plasmas* **26** 022706

[33] Hansen E C *et al* 2020 Neutron yield enhancement and suppression by magnetization in laser-driven cylindrical implosions *Phys. Plasmas* **27** 062703

[34] Walsh C A, Chittenden J P, Hill D W and Ridgers C 2020b Extended-magnetohydrodynamics in under-dense plasmas *Phys. Plasmas* **27** 022103

[35] Gao L, Nilson P M, Igumenshchev I V, Haines M G, Froula D H, Betti R and Meyerhofer D D 2015 Precision mapping of laser-driven magnetic fields and their evolution in high-energy-density plasmas *Phys. Rev. Lett.* **114** 215003

[36] Campbell P T, Walsh C A, B k Russell, J P Chittenden, Crilly A, Fiksel G, Nilson P M, Thomas A G R, Krushelnick K, and Willingale L 2020 Magnetic signatures of radiation-driven double ablation fronts, *Phys. Rev. Lett.* **125** 145001

[37] Tubman E R *et al* 2021 Observations of pressure anisotropy effects within semi-collisional magnetized plasma bubbles *Nat. Commun.* **12** 334

[38] Joglekar A S, Ridgers C P, Kingham R J and Thomas A G R 2016 Kinetic modeling of Nernst effect in magnetized hohlraums *Physi. Rev.* E **93** 043206

[39] Hill D W and Kingham R J 2017 Enhancement of pressure perturbations in ablation due to kinetic magnetised transport effects under direct-drive ICF relevant conditions (arxiv:1712.02663)

[40] Sherlock M and Bissell J J 2020 Suppression of the Biermann battery and stabilization of the thermomagnetic instability in laser fusion conditions *Phys. Rev. Lett.* **124** 055001

[41] Walsh C, Chittenden J, McGlinchey K, Niasse N and Appelbe B 2017 Self-generated magnetic fields in the stagnation phase of indirect-drive implosions on the national ignition facility *Phys. Rev. Lett.* **118** 155001

[42] Regan S P *et al* 2002 Characterization of direct-drive-implosion core conditions on omega with time-resolved Ar K-shell spectroscopy *Phys. Plasmas* **9** 1357

[43] Welser-Sherrill L *et al* 2007 Spectroscopic determination of temperature and density spatial profiles and mix in indirect-drive implosion cores *Phys. Rev.* E **76** 056403

[44] Florido R, Mancini R C, Nagayama T, Tommasini R, Delettrez J A, Regan S P and Yaakobi B 2011 Measurements of core and compressed-shell temperature and density conditions in thick-wall target implosions at the omega laser facility *Phys. Rev.* E **83** 066408

[45] Florido R, Mancini R C, Nagayama T, Tommasini R, Delettrez J A and Regan S P 2014 Time-resolved characterization and energy balance analysis of implosion core in shock-ignition experiments at omega *Phys. Plasmas* **21** 102709

[46] Nagayama T, Mancini R C, Florido R, Mayes D, Tommasini R, Koch J A, Delettrez J A, Regan S P and Smalyuk V A 2014 Direct asymmetry measurement of temperature and density spatial distributions in inertial confinement fusion plasmas from pinhole space-resolved spectra *Phys. Plasmas* **21** 050702

[47] Carpenter K R, Mancini R C, Harding E C, Harvey-Thompson A J, Geissel M, Weis M R, Hansen S B, Peterson K J and Rochau G A 2020a Magnetic field impact on the laser heating in maglif *Phys. Plasmas* **27** 052704

[48] Carpenter K R, Mancini R C, Harding E C, Harvey-Thompson A J, Geissel M, Weis M R, Hansen S B, Peterson K J and Rochau G A 2020b Temperature distributions and gradients in laser-heated plasmas relevant to magnetized liner inertial fusion *Phys. Rev.* E **102** 023209

[49] Ciardi A *et al* 2007 The evolution of magnetic tower jets in the laboratory *Phys. Plasmas* **14** 056501

[50] Chittenden J P, Lebedev S V, Jennings C A, Bland S N and Ciardi A 2004 X-ray generation mechanisms in three-dimensional simulations of wire array Z-pinches *Plasma Phys. Control. Fusion* **46** B457

[51] Sadler J D, Walsh C A and Li H 2021 Symmetric set of Transport coefficients for collisional magnetized plasma *Phys. Rev. Lett.* **126** 075001

[52] Walsh C A and Clark D S 2021 Biermann battery magnetic fields in ICF capsules: total magnetic flux generation *Phys. Plasmas* **28** 092705

[53] Campbell P T *et al* 2022 Measuring magnetic flux suppression in high-power laser–plasma interactions *Phys. Plasma* **29** 012701

[54] Sadler J D, Li H and Flippo K A 2020 Magnetic field generation from composition gradients in inertial confinement fusion fuel *Phil. Trans. R. Soc.* A **378** 20200045

[55] Walsh C A, Sadler J D and Davies J R 2021 Updated magnetized transport coefficients: impact on laser-plasmas with self-generated or applied magnetic fields *Nucl. Fusion* **61** 116025

[56] Epperlein E M and Haines M G 1986 Plasma transport coefficients in a magnetic field by direct numerical solution of the Fokker-Planck equation *Phys. Fluids* **29** 1029

[57] Sharma P and Hammett G W 2007 Preserving monotonicity in anisotropic diffusion *J. Comput. Phys.* **227** 123–42

[58] Walsh C A 2018 Extended magneto-hydrodynamic effects in indirect-drive inertial confinement fusion experiments *PhD Thesis* Imperial College London

[59] Jennings C 2006 Radiation transport effects in wire array Z pinches and magneto-hydrodynamic modelling techniques *PhD Thesis* Imperial College London

[60] Hansen E C *et al* 2018b Measuring implosion velocities in experiments and simulations of laser-driven cylindrical implosions on the OMEGA laser *Plasma Phys. Control. Fusion* **60** 054014

[61] MacFarlane J 2003 VISRAD—a 3-D view factor code and design tool for high-energy density physics experiments *J. Quant. Spectrosc. Radiat. Transfer* **81** 287

[62] Betti R, Umansky M, Lobatchev V, Goncharov V N and McCrory R L 2001 Hot-spot dynamics and deceleration-phase Rayleigh-Taylor instability of imploding inertial confinement fusion capsules *Phys. Plasmas* **8** 5257

[63] Davies J R, Betti R, Chang P-Y and Fiksel G 2015 The importance of electrothermal terms in Ohm's law for magnetized spherical implosions *Phys. Plasmas* **22** 112703

[64] Huba J B 2013 *NRL Formulary*

[65] Perkins L J, Logan B G, Zimmerman G B and Werner C J 2013 Two-dimensional simulations of thermonuclear burn in ignition-scale inertial confinement fusion targets under compressed axial magnetic fields *Phys. Plasmas* **20** 0

[66] Haines M G 1986 Heat flux effects in Ohm's law *Plasma Phys. Control. Fusion* **28** 1705

[67] Braginskii S I 1965 Transport processes in a plasma *Rev. Plasma Phys.* **1** 205–205

[68] Seyler C E, Martin M R and Hamlin N D 2018 Helical instability in MagLIF due to axial flux compression by low-density plasma *Phys. Plasmas* **25** 062711

[69] Chittenden J P and Haines M G 1993 Nernst and Ettinghausen effects in the dense Z-pinch: their impact upon equilibria and runaway electrons *J. Phys. D: Appl. Phys.* **26** 1048

[70] Hamlin N D, Seyler C E and Khiar B 2018 The influence of the Hall term on the development of magnetized laser-produced plasma jets *Phys. Plasmas* **25** 042906

[71] Bell A R, Kingham R J, Watkins H C and Matthews J H 2020 Instability in a magnetised collisional plasma driven by a heat flow or a current *Plasma Phys. Control. Fusion* **62** 095026

[72] Appelbe B and Chittenden J 2014 Relativistically correct DD and DT neutron spectra *High Energy Density Phys.* **11** 30

[73] Gigosos M A, González-Herrero D, Lara N, Florido R, Calisti A, Ferri S and Talin B 2018 Classical molecular dynamics simulations of hydrogen plasmas and development of an analytical statistical model for computational validity assessment *Phys. Rev. E* **98** 033307

[74] Joshi T R 2015 Hydrodynamic stability and Ti-tracer distribution in low-adiabatic OMEGA direct-drive implosions *PhD Thesis* University of Nevada, Reno

[75] Florido R, Rodríguez R, Gil J M, Rubiano J G, Martel P, Mínguez E and Mancini R C 2009 Modeling of population kinetics of plasmas that are not in local thermodynamic equilibrium, using a versatile collisional-radiative model based on analytical rates *Phys. Rev. E* **80** 056402

[76] Florido R, Mancini R, Nagayama T, Tommasini R, Delettrez J, Regan S, Smalyuk V, Rodríguez R and Gil J 2010 Argon k-shell and bound-free emission from omega direct-drive implosion cores *High Energy Density Phys.* **6** 70

[77] Fontes C J *et al* 2015 The Los Alamos suite of relativistic atomic physics codes *J. Phys. B: At. Mol. Opt. Phys.* **48** 144014

[78] Gu M F 2008 The flexible atomic code *Can. J. Phys.* **86** 675

[79] Stewart J C, Pyatt J and Kedar D 1966 Lowering of ionization potentials in plasmas *Astrophys. J.* **144** 1203

[80] Mancini R C, Joyce R F and Hooper C F 1987 Escape factors for stark-broadened line profiles *J. Phys. B: At. Mol. Phys.* **20** 2975

[81] Mancini R, Kilcrease D, Woltz L and Hooper C 1991 Calculational aspects of the stark line broadening of multielectron ions in plasmas *Comput. Phys. Commun.* **63** 314

[82] Boercker D B, Iglesias C A and Dufty J W 1987 Radiative and transport properties of ions in strongly coupled plasmas *Phys. Rev. A* **36** 2254

[83] Gigosos M A, Mancini R C, Martín-González J M and Florido R 2021 Stark-broadening of Ar k-shell lines: a comparison between molecular dynamics simulations and MERL results *Atoms* **9** 9

[84] Geller D K and Weisheit J C 1997 Classical electron-ion scattering in strongly magnetized plasmas. I. A generalized Coulomb logarithm *Phys. Plasmas* **4** 4258–71